NASA Technical Memorandum 101081

A Long-Range Laser Velocimeter for the National Full-Scale Aerodynamics Complex: New Developments and Experimental Application

Michael S. Reinath

(NASA-TM-101081) A LONG-RANGE LASER VELOCIMETER FOR THE NATIONAL FULL-SCALE AERODYNAMICS COMPLEX: NEW DEVELOPMENTS AND EXPERIMENTAL APPLICATION (NASA. Ames Research Center) 44 p CSCL 14B G3/35

N89-26207

Unclas
0219619

June 1989

National Aeronautics and
Space Administration

NASA Technical Memorandum 101081

A Long-Range Laser Velocimeter for the National Full-Scale Aerodynamics Complex: New Developments and Experimental Application

Michael S. Reinath, Ames Research Center, Moffett Field, California

June 1989

NASA

National Aeronautics and
Space Administration

Ames Research Center
Moffett Field, California 94035

SYMBOLS

a_1	constant term in autocorrelation function (depends on number of particles, geometry, and duration of data-gathering)
B	beam separation distance at output aperture
b	background level of autocorrelation function
f	Doppler frequency (including acousto-optic offset frequency)
f_o	offset frequency generated by acousto-optic shifting
f_s	Doppler frequency shift, $f - f_o$
$F(\tau)$	modified autocorrelation function, $\left\{\frac{H(\tau) - b}{\Psi(\tau)} - 1\right\}$
g(u)	function defined as $\frac{m^2}{2} P_u(u)$
h(f)	function defined as $g(\delta_f f)$
$H(\tau)$	autocorrelation function
I	photomultiplier current (photon-saturated case), or probability of photon detection by photocathode (photon resolved case)
m	Michelson fringe visibility
N	number of samples acquired
N_{fr}	number of fringes in measuring volume
N_{fft}	time record array length for fast Fourier transformation
$P_u(u)$	probability density function which characterizes the mean and turbulence of the u-velocity component
$P_{uv}(u,v)$	probability density function which characterizes the mean and turbulence of the u- and v-velocity components
R	distance from output aperture to measuring volume

r_o	beam radius at waist (1/e)
S_u	estimator of the standard deviation of the u-distribution
ΔS	uncertainty interval associated with the estimator of the standard deviation (statistical or systematic)
t	time
Δt_c	counter processor clock cycle, 2 nsec
u, v	orthogonal velocity components
u_i	instantaneous, single-particle u-component velocity
$\overline{U}, \overline{V}$	mean values of the velocity components u and v
$\overline{u'^2}$	estimator of the turbulent kinetic energy in the u-direction
Δu	uncertainty interval associated with the u-component of velocity (statistical or systematic)
Z_c	confidence coefficient, 1.96 for 95% confidence level
β	beam convergence angle
δ_f	fringe spacing
$\Phi(\tau)$	function defined as $F(\tau)/\delta_f$
λ	laser wavelength, 514.5 or 488.0 nm
ρ	ratio of beam amplitudes
σ_u	true standard deviation of the u-distribution
τ	delay increment for autocorrelation
$\Psi(\tau)$	beam profile shape term, $a_1 \text{EXP}\left[-\frac{(\overline{U}^2 + \overline{V}^2)\tau^2}{r_o^2}\right]$

SUMMARY

A long-range laser velocimeter (LV) developed for remote operation from within the flow fields of the large wind tunnels of the National Full-Scale Aerodynamics Complex is described. Emphasis is placed on recent improvements in optical hardware as well as recent additions to data acquisition and processing techniques. The system has been upgraded from a dual-beam, single-color LV with focal range to 10 m, to a dual-beam, two-color LV with focal range to 20 m. At the new extended measurement range (between 10 and 20 m), signals are photon-resolved, and a photon correlation technique is applied to acquire and process the LV signals. This technique permits recovery of the velocity probability distributions at a particular measurement location from which the mean components of velocity and the corresponding normal stress components of turbulence are obtained. The method used for data reduction is outlined in detail, and a discussion of measurement accuracy is made. To study the performance of the LV and verify the measurement accuracy, laboratory measurements were made in the flow field of a 10-cm-diameter, 30-m/sec axisymmetric jet. Measurements were taken at locations two and four diameters downstream of the exit and at measurement ranges to 10 and 20 m using conventional and photon-correlation data-reduction techniques, respectively. These measured velocity and turbulence intensity surveys are compared to measurements made with a hot-wire anemometer. Additionally, the LV was used during the flow calibration of the 80- by 120-Foot Wind Tunnel to measure the test-section boundary-layer thickness at the maximum wind tunnel speed of 51.5 m/sec. A discussion of the requirements and techniques used to seed the flow is made, and boundary-layer surveys of mean velocity and turbulence intensity of the streamwise component and the component normal to the surface are presented. The streamwise component of mean velocity is compared to data obtained with a total pressure rake.

INTRODUCTION

Wind tunnel velocity measurements are made routinely to provide data for aerodynamic research. A wide variety of measuring tools have been devised for this purpose ranging from the simple tuft, which provides only qualitative data, to more complex instruments such as the cup anemometer, the multihole pitot probe, the hot-wire anemometer, and the laser velocimeter (LV). Each of these measuring devices has inherent advantages and disadvantages, and the usefulness of each device is dependent on the specific research application.

Almost every measurement tool for measuring wind tunnel velocity relies on a sensor element mounted within the flow. This element occupies some physical space at the measurement location, and its use creates a need for a support structure that must withstand the wind tunnel dynamic pressure. Depending on the particular application, this sensor element and support hardware can introduce potentially significant flow perturbations in the velocity field at and around the measurement location.

The LV, however, does not rely on a sensor element at the measurement location, and therefore does not require the use of any support hardware in the vicinity of the measurement. This is advantageous, for example, around rotating blades where the use of sensors and support hardware is not feasible or desirable.

A number of inherent disadvantages arising from its complex nature make the LV more difficult to use, however. Use of an LV often requires more highly trained operators, more complex data processing, and longer measurement times. The LV is, consequently, not suitable for all applications, and simpler, more basic instrumentation is often adequate for many velocity measurements.

One application for which the remote measurement capability of the LV is sometimes suitable is the measurement of velocity in large aerodynamic test facilities. This type of measurement can be particularly challenging, especially when large regions of the flow are of interest. When mechanical probes are used, large rake assemblies and associated support hardware, together with bulky translation mechanisms, must often be constructed (ref. 1). Although data can be acquired at many spatial flow-field positions simultaneously or in rapid succession using this technique, the measurement hardware is usually test-specific and only partially reusable, if at all.

When the LV is employed, data must be acquired in backscatter over long distances. Long-range backscatter LV measurements are difficult to acquire and process because of the relatively low signal level associated with the backscatter mode of operation. The need to translate the measurement location within the flow adds to the complexity, and much time can be consumed in mapping a region since the LV is limited to a point-by-point measurement.

An LV system which deals with these challenges has been designed at NASA's Ames Research Center for use in large facilities. Reference 2 provides a description of the LV system status as of January 1984. Since that time, major modifications have been made to expand the system's capabilities. A second color has been added so that data can be acquired simultaneously on two channels, and the focal range has been extended from 10 m to 20 m. A description of the new hardware and the extended range of operation follows.

SYSTEM HARDWARE

General

The LV described herein is designed for use in the facilities of the National Full-Scale Aerodynamics Complex (NFAC), and is designated the Long-Range Laser Velocimeter (LRLV). A typical measurement application is shown in figure 1 at the NFAC Outdoor Aerodynamic Research Facility where vertical/short takeoff and landing (VSTOL) hover testing is often conducted.

A cutaway diagram of the instrument is shown in figure 2. The instrument's streamlined external shape minimizes the flow perturbation produced when it is placed in the wind tunnel test-section flow field. In smaller facilities, LV systems are normally mounted external to the flow, and optical access is

provided by test section windows. This arrangement is impractical in facilities as large as those of the NFAC, where backscatter measurement ranges would quickly become excessive. Therefore, it was decided to place the velocimeter system on the floor inside the wind tunnel test section. The advantage of the LV measurement technique in being nonintrusive is thus potentially compromised; however, computations by Reinath and Ross (ref. 3) have shown that the interference is significant only close to the LRLV.

The LRLV is capable of measuring two orthogonal components of velocity with a two-color, double-dual-beam optical configuration. Stepper motors and absolute encoders are used under computer control to position the test point within the flow field. A third orthogonal component of velocity can be obtained by a transformation of coupled velocity components (ref. 2).

Transmitting Optics

An argon-ion laser head operating in the broad-band mode generates an output beam of nominally 18 W maximum continuous power. This beam immediately enters a three-prism assembly, shown in figure 3, which disperses the colors of the argon broad-band beam. Each equilateral prism is positioned at the angle which causes the minimum angular displacement of the transmitted beam to minimize the total angular displacement through all three prisms. This angle is 60.1° for the 514.5-nm line and 60.7° for the 488.0-nm line (through a single prism). Through the entire set, angular displacements are 180.3° and 182.2° for the 514.5-nm and 488.0-nm lines, respectively. The resulting dispersion is 1.90° between the two beams.

The diverging beams are separated farther by three dielectrically coated mirrors (fig. 3) before entering a pair of beam-expanding telescopes. These telescopes expand the 2-mm-diameter input beams to a diameter of 4 mm using two simple, single-element, plano-convex lenses each. A sharper focus is thereby produced at the measuring volume within the flow.

The 514.5-nm beam (green) and the 488.0-nm beam (blue) are each split into two beams of equal intensity by two beam splitters located down-beam of the beam-expanding telescopes. A quarter-wave plate located ahead of the first beam splitter rotates the polarization of the green beam by 90° before it is split in the horizontal plane by this beam splitter. The resulting parallel beam pair, spaced 50 mm apart, passes through clearance holes in the second beam splitter. The blue beam is directed into the second beam splitter by a pair of dielectrically coated mirrors (fig. 3), where it is split in the vertical plane.

Each of the four beams is then frequency-shifted by four acousto-optic cells, driven at frequencies of 44.0 and 52.0 MHz, before passing through the final focusing optics (fig. 3). Frequency-shifting eliminates directional ambiguity by creating an 8-MHz zero-offset frequency, and increases the number of cycles per Doppler burst for a given particle velocity. The dual-cell configuration is used to facilitate filtering of the Doppler signal by ensuring separation of the signal frequency from any radio frequency radiation generated by the cell-driver electronics. Each acousto-optic cell has an acoustic field height of 5 mm, is designed to tolerate a continuous beam power of 4.5 W, and operates at a diffraction efficiency of 88% into the first order. The optical substrate of each cell was selected during manufacture for negligible birefringence throughout the clear aperture of the cell—during development, many acousto-optic cells were found to have birefringent properties which varied with beam position through the substrate

and disrupted the linear polarization of the beams. During manufacture, care was also taken to mount the optical substrate so that no significant birefringence would be created by mechanical strain of the cell housing or mounting supports.

The frequency-shifted beams are then focused to a point in the flow field by one of two interchangeable, three-module zoom lens systems (fig. 2). Focal distances ranging from 2.6 to 10 m and from 10 to 20 m can be reached by selecting the appropriate set. Each set consists of two separate singlet elements and a movable triplet assembly. The two output singlets have clear apertures of 33 cm and 34 cm, respectively. Spherical and longitudinal chromatic aberrations have been corrected at the two argon wavelengths to maintain sharp imagery over the focal range.

A large folding mirror (fig. 2) is used to reflect the beams into the flow field. The 6.4-cm-thick mirror weighs about 30 kg and is dielectrically coated for maximum reflectance (99.94%) at the argon wavelength and 45° of incidence.

Receiving Optics: 2.6- to 10-m Focus

Light is scattered in all directions when particles moving with the flow field pass through the measuring volume illuminated by the transmitted beams. Some of this light is collected by the receiving optics. Specifically, only the rays that fall within the bounds of an imaginary cone formed by rotation of the transmitted beam pairs about their optical axis are collected. These rays pass through the same lens system that is used for transmission and emerge as parallel light. They are then reflected by an elliptical dielectric mirror inclined at 45° to the optical axis, as shown in figure 4. A simple plano-convex lens focuses the parallel rays, and a dichroic mirror separates the colors by reflecting one color while allowing the other to pass through (the 488.0-nm wavelength is reflected). The light is then imaged at a 0.5-mm pinhole and filtered by a narrow band-pass interference filter at each photomultiplier tube. No translation of the photomultiplier tubes is necessary to maintain focus of the images over this focus range.

Receiving Optics: 10- to 20-m Focus

An isolated collection lens is used to improve noise immunity for 10- to 20-m focal ranges. This lens is a stationary, three-element assembly that is mounted coaxially with the transmission lenses, as shown in figure 5. Scattered light is collected through its 20.3-cm clear aperture and is focused at about 40.0 cm. A dichroic mirror separates the two colors ahead of the photomultiplier tubes. The collected light is imaged at 0.5-mm-diameter pinholes and transmitted through band-pass interference filters before entering the photomultiplier tubes.

The phototube assemblies are positioned to maintain focus of the images at the pinholes over the zoom range. Positioning is accomplished using a stepper-motor-driven translation stage with absolute encoder readback. The position is slaved through software to the zoom position of the transmitting optics. A 1.3-cm displacement is required to maintain focus when the transmission optics are zoomed from 10 to 20 m.

Onboard Data-Acquisition and Control Instrumentation

Four stepper motors and electronic drivers position the test point within the flow field as shown in figure 6. Two are dedicated to generating the displacements required for optical zoom of the transmission and collection optics. The third is dedicated to translating the system laterally along support rails mounted on the floor. The fourth is dedicated to providing rotational translation about the upper assembly axis of rotation (fig. 2). Four 15-bit, absolute, optical shaft angle encoders provide the feedback necessary for accurate positioning of the motors.

An onboard controller is linked through a computer interface to the main computer and to the onboard components shown in figure 6. Commands are sent through the interface to the onboard controller. The controller can be instructed to signal the main computer when a requested operation is complete so that the main computer is not forced to wait unnecessarily. Parameters under control are motor speeds (variable with ramped acceleration and deceleration), motor positions, encoder readbacks, and photomultiplier high voltages.

The motors can be actuated manually from a control panel which is part of the onboard hardware (fig. 6). Another control panel can be used, locally or remotely, for position adjustment of the dichroic and dielectric mirrors that direct the return light to the photomultiplier pinholes. This feature is important during operation, when thermal drift and mechanical vibration can cause slight misalignment of the image at the phototube pinholes (small adjustments are made while improvement of signal quality on the data-acquisition instrumentation is closely monitored).

Remote Data-Acquisition and Control Instrumentation

A diagram showing the components of the remote data-acquisition and control instrumentation is presented in figure 7. The main computer is interfaced to the peripherals shown and to the computer interface that is linked to the onboard controller. Data are supplied to the computer from either of two instruments: the signal processors or the high-speed correlator. When data are acquired with the shorter-focal-range receiving optics, signals are photon-saturated, and the counter-type signal processors are used. The high-speed correlator is required when the longer-focal-range receiving optics are used; signals acquired over these focal distances are composed of photon-resolved pulses and cannot be processed using the counters.

The spectrum analyzer, pulse-height analyzer, and oscilloscope, shown in the figure, are used to monitor the photon-saturated signals and evaluate signal quality. Adjustment of the filter settings and threshold level on the counter processors is made using feedback obtained from these instruments.

Laser power is adjusted at a custom, remote laser control panel. The panel is equipped with readout of the beam power in watts, and diagnostic panel lights necessary for monitoring correct system function. The laser can be activated or deactivated at the panel, and a key control protects against unauthorized use.

Measurement Resolution

A summary of the overall system measurement resolution follows. The discussion focuses on three factors that are important in determining system performance: mechanical positioning of the focal volume, size of the focal volume, and spacing of the interference fringes.

The system measurement resolution is determined, in part, by how accurately the focal volume can be positioned in the flow field. Stepper motor drive assemblies equipped with 15-bit shaft-angle encoders establish this positioning resolution, as described in reference 2. Vibration of the instrument and hysteresis in the drive assemblies can introduce significant uncertainty. Vibrations are minimized with the aid of isolation mounts, but some loss of resolution must be tolerated. Hysteresis can be controlled in software, and its effects are essentially eliminated.

The measurement resolution is also affected by the size of the focal volume, especially its length. The fineness ratio of the ellipsoidal focal volume ranges from 30 at a focal distance of 2.6 m to 80 at a focal distance of 20 m. Measurements of the focal volume size were made at several focal distances. The results are plotted in figures 8 and 9. Figure 8 shows diameter intensity profiles at two focal distances, 6.3 and 15 m—the two mid-zoom distances. At these distances, about 15 interference fringes are present in the focal volume spaced at 12.7 and 27.5 μm, respectively. The length and diameter at other focal ranges is shown in figures 9(a) and 9(b), where these parameters are plotted as a function of zoom. Length of the focal volume can become significant when local layers of high shear become thin enough to impose velocity gradients across the volume. A spatial averaging of the gradient then takes place during the measurement. Under these conditions, the true gradient may not be correctly resolved because an effective broadening of the layer occurs as a result of the spatial averaging.

The spacing of the interference fringe pattern effectively determines the instrument's ability to resolve incremental changes in the measured velocity for a particular method of signal processing. The larger the spacing of the fringes, the more difficult it is to resolve small changes. Unfortunately, fringe patterns are generally spaced more widely for long-range measurement configurations because a shallower beam-convergence angle is usually necessary. The present configuration is no exception. At the two respective mid-zoom distances, the LRLV fringe pattern is spaced at 12.7 and 27.5 μm. The associated sensitivity to incremental changes in velocity is 78.7 and 36.4 kHz of Doppler shift per 1 m/sec of change in velocity, respectively. The final velocity resolution of the instrument depends on the ability of the processing techniques to resolve these small changes in Doppler frequency. Further discussion is presented in the section dealing with measurement uncertainty.

System specifications are presented in table I.

DATA REDUCTION: THEORETICAL CONSIDERATIONS

Photon-Saturated Signals

Doppler bursts acquired using the shorter-focal-length optics are photon-saturated. A continuous photomultiplier signal therefore is present within each burst, and counter-type processing techniques are used to measure the Doppler frequency. This frequency is converted to velocity by using the expression

$$u = \frac{\lambda(f - f_o)}{2 \sin \beta/2} \tag{1}$$

where f is the measured Doppler frequency, including the offset due to shifting. A number of velocity samples, N, are normally acquired at a particular location of interest in the flow field. An estimator of the mean velocity is then computed using the ensemble average

$$\overline{U} = \frac{1}{N} \sum_{i=1}^{N} u_i \tag{2}$$

The normal stress component of turbulence, $\overline{u^2}$, is calculated using the true variance of the distribution, σ_u^2, assuming that any statistical variations of the measured velocity samples about the mean value caused by effects other than turbulence are insignificant. An estimator of the true variance is obtained by using the expression

$$S_u^2 = \frac{1}{N} \sum_{i=1}^{N} (u_i - \overline{U})^2$$

where the symbol S is used instead of σ to emphasize that S_u^2 is strictly only an estimator of σ_u^2. For computational purposes, this equation can be rewritten as

$$S_u^2 = \frac{1}{N-1} \left(\sum_{i=1}^{N} u_i^2 - N\overline{U}^2 \right) \tag{3}$$

in order to reduce the time required for the repetitive calculation with large ensembles.

Photon-Resolved Signals

Doppler bursts acquired using the longer-focal-length optics are photon-resolved. The photomultiplier signal therefore is no longer continuous within each burst, and counter-type processing techniques cannot be used for data reduction. In the following section, the technique used to process photon resolved signals is outlined.

The photomultiplier current generated when particles traverse the measuring volume has been expressed as a function of time (refs. 4-9). For the case when signals are photon-saturated, this function represents the photomultiplier current and is a continuous function of time. For the case when signals are photon-resolved, however, the current is not continuous, but is composed of discrete pulses. In this case, instead of representing the actual photomultiplier current, the same function represents the probability of photon detection by the photocathode as a function of time. To extract the Doppler frequency, the time-varying photomultiplier current is autocorrelated by a correlator instrument. The output is proportional to the function

$$H(\tau) = \int_{-\infty}^{\infty} I(t)I(t+\tau)dt$$

The function $H(\tau)$ is called the autocorrelation function of the signal I(t). This function has been derived for a large number of particle transits in a turbulent flow by Abbiss (refs. 4-7) and is expressed as follows:

$$H(\tau) = a_1 \int_{-\infty}^{\infty}\int_{-\infty}^{\infty} P_{uv}(u,v)\,\mathrm{EXP}\left[\frac{(u^2+v^2)\tau^2}{r_o^2}\right]\left(1+\frac{1}{2}m^2\cos\frac{2\pi u\tau}{\delta_f}\right)du\,dv \qquad (4)$$

The following assumptions are made by Abbiss in deriving this equation: (1) the measuring volume is approximated by a cylinder; (2) the probability is low for particle transits that have large particle velocities along the axis of the cylinder; and (3) the beam-intersection angle is small. To simplify the expression, Abbiss makes two additional assumptions : (1) $P_{uv}(u,v)$ is not separable to account for the effect of shear; and (2) turbulence is low so that the u and v distributions are narrow (the variables u and v can then be replaced in the exponential term by their mean values $\overline{U}$ and $\overline{V}$). The exponential term can be moved outside the integral, and the integration can be carried out with respect to v. Noting that

$$\int_{-\infty}^{\infty} P_{uv}(u,v)dv = P_u(u)$$

equation (4) reduces to (refs. 4-7)

$$H(\tau) = a_1\,\mathrm{EXP}\left[-\frac{(\overline{U}^2+\overline{V}^2)\tau^2}{r_o^2}\right]\int_0^{\infty} P_u(u)\left(1+\frac{1}{2}m^2\cos\frac{2\pi u\tau}{\delta_f}\right)du \qquad (5)$$

The lower limit of integration is set equal to zero because frequency shifting ensures that u never assumes a negative value.

The autocorrelation function, $H(\tau)$, can be modified (ref. 10) by subtracting from it the background level of the autocorrelator output and dividing the result by the constant exponential term that represents the beam intensity profile contribution to the shape of the autocorrelation function. Equation (5) then becomes

$$\left[\frac{H(\tau)-b}{\Psi(\tau)}-1\right]=\frac{m^2}{2}\int_0^\infty P_u(u)\cos\frac{2\pi u\tau}{\delta_f}\,du \tag{6}$$

where $\Psi(\tau)$ represents the beam profile. By defining two new functions,

$$F(\tau)=\left[\frac{H(\tau)-b}{\Psi(\tau)}-1\right]$$

and

$$g(u)=\frac{m^2}{2}P_u(u)$$

equation (6) can be written in a more compact form as

$$F(\tau)=\int_0^\infty g(u)\cos\frac{2\pi u\tau}{\delta_f}\,du \tag{7}$$

This equation can be transformed into the general expression for the Fourier transformation of an even function (ref. 11) by letting $f = u/\delta_f$ to give

$$\Phi(\tau)=\int_0^\infty h(f)\cos(2\pi f\tau)df \tag{8}$$

where $\Phi(\tau)$ and $h(f)$ are defined as the functions $F(\tau)/\delta_f$ and $g(\delta_f f)$, respectively. The functions $\Phi(\tau)$ and $h(f)$ are a Fourier transform pair (ref. 11), where

$$\Phi(\tau)=\frac{1}{\delta_f}\left[\frac{H(\tau)-b}{\Psi(\tau)}-1\right] \tag{9}$$

and

$$h(f)=\frac{m^2}{2}P_u(u) \tag{10}$$

The function h(f) differs from the u-velocity probability-density distribution by the constant $m^2/2$, where m is the Michelson fringe visibility. The Michelson fringe visibility can be obtained by integration of equation (10) over the frequency domain

$$\int_0^\infty h(f)df = \frac{m^2}{2}\int_0^\infty P_u(u)du$$

which reduces to

$$m = \left[2\int_0^\infty h(f)df\right]^2$$

Recovery of the $P_u(u)$ distribution, the end product of the measurement yielding mean velocity and turbulence intensity, can be simplified by omitting the division by δ_f in equation (9). The inverse Fourier transform of the modified autocorrelation function is then related to the $P_u(u)$ distribution by some arbitrary unimportant constant, instead of by the fringe visibility. The distribution is normalized for convenience, and the mean value and variance are determined using the methods described in the next section.

DATA REDUCTION: PRACTICAL TECHNIQUES

The practical techniques used to process photon-resolved data are taken from the work of Durst et al. (refs. 12 and 13) and Sharp (ref. 10). A brief description of these techniques is given in this section. No description of the techniques used to reduce photon-saturated data is presented here, however. A complete description of these techniques is given in reference 2.

A schematic overview of the reduction process similar to that given by Durst is presented in figures 10(a) and 10(b). Particles passing through the focal volume generate the photomultiplier current pulses shown. These pulses are conditioned by the discriminator before being supplied to the high-speed digital correlator. Very weak and very strong pulses are rejected by adjusting a window-mode threshold control on the discriminator unit. The resulting pulses are then processed by a correlator to produce an autocorrelation function that is 256 delay increments in length with a minimum delay increment of 5 nsec.

A distortion of the correlogram due to the inherent dead-time of the photomultiplier tube extends to the fifth or sixth correlation coefficient, at the minimum 5-nsec delay time. This distortion is corrected by using a linear approximation for the first estimate of velocity, as shown in figure 10(b). After correction of the distortion, a least-squares linear fit is first calculated to approximate the beam profile, and subtracted (refs. 12 and 13), and then a dedicated, high-speed, parallel-processor board within the computer calculates the Fast Fourier Transformation (FFT). An automatic search is then made for the peak in the frequency domain between two limits that can be changed interactively by the experimenter, simila

to filter settings on a signal conditioner (fig. 10(b)). The time required for the search is thereby reduced and the first estimate of the Doppler frequency is effectively band-pass-filtered.

This first estimate is used to make a second correction of the correlogram distortion using the method suggested by Sharp (ref. 10). First, the correlogram is folded about zero to generate an even function and padded with zeros to a length of 1024 (fig. 10(b)). Then a 9-msec FFT is calculated by a parallel processor, and a peak search is conducted between the selected filter limits. Subsequently, a parabolic curve fit of the peak value and the two adjacent points is made to improve the resolution, as suggested by Durst (refs. 12 and 13). Finally, a signal-to-noise ratio is calculated by dividing the peak Doppler value by the second highest peak value located between the filter limits. The result is output to the screen.

When turbulence is of interest, the velocity probability distribution of equation (5) is recovered by applying a cosine transformation. First, the original correlogram is used to calculate a Gaussian beam profile. This profile is then divided into the original correlogram after subtraction of the background level to obtain the modified autocorrelation function of equations (6) and (7). The transformation yields the probability distribution, in terms of frequency, which is then used to compute the mean and apparent standard deviation.

This standard deviation may be larger than the actual value, because of the truncation effect of the finite correlogram length at low turbulence levels. This is because the oscillations of the correlogram may not have decayed sufficiently to zero by the end of the record. Abbiss (ref. 4) reports that broadening effects begin to appear below a turbulence level of about 4% to 5% for a 48-channel correlator. He presents a correction scheme which is discussed further in the appendix.

MEASUREMENT UNCERTAINTY

Systematic Uncertainty

An expression relating the overall relative systematic uncertainty to the measured parameters and their relative uncertainties (refs. 2 and 14) is given by

$$\frac{\Delta u}{u} = \frac{\Delta f}{f_s} + \cos^2\left(\frac{\beta}{2}\right)\frac{\Delta R}{R} + \left[1 + \sin^2\left(\frac{\beta}{2}\right)\right]\frac{\Delta B}{B} \tag{11}$$

This expression applies whether counter processor or photon correlation techniques are used. The first term on the right-hand side is the relative uncertainty of the measured frequency. When a counter processor is used to acquire data, the value of this term is determined by the finite resolution of the counter's internal clock cycle, Δt_c. The value of Δf is given by the expression (ref. 15)

$$\Delta f = \frac{f^2 \Delta t_c}{N_{fr}}$$

for an individual, single-particle measurement. The counter processor, however, is generally used to acquire an ensemble of single-particle measurements at a given measurement location. Each individual measurement therefore has its own random $\Delta f/f_s$ uncertainty due to the clock count resolution. This uncertainty contributes to the broadening of the ensemble distribution. It does not affect the value of the mean, however, because the term $\Delta f/f_s$ averages to zero for sufficient sample size because of the random nature of the clock count uncertainty.

When signals are processed using photon correlation, on the other hand, the term $\Delta f/f_s$ does not drop from the expression for $\Delta u/u$. Δf is determined by the resolution of the FFT, in this case, and is given by the expression (ref. 11)

$$\Delta f = \frac{1}{\tau k N_{fft}} \tag{12}$$

where $N_{fft} = 1024$ and $k = 2$ for the case where the peak frequency is determined using the parabolic fit. The improved resolution is a result of using the parabolic fit to get the peak frequency (ref. 12).

The second and third terms in equation (11) are small, but are included in the estimate of combined uncertainty which follows the next section.

Statistical Uncertainty

In turbulent flow, repeated single-particle LV measurements can be made to build a distribution of instantaneous velocity values at a location of interest. Estimators of the mean and standard deviation of a distribution are then calculated using equations (2) and (3) or equation (8), depending on the signal level and method of data reduction used. The statistical uncertainties of these parameters are expressed as uncertainty intervals within the bounds of which the true values are expected to fall. The uncertainty intervals are given by the equations

$$\Delta u = \pm \frac{Z_c S_u}{\sqrt{N}} \tag{13}$$

and

$$\Delta S = \pm \frac{Z_c S_u}{\sqrt{2N}}$$

for large N (N greater than about 30) (refs. 16-19). The distribution of velocity values may deviate from the normal distribution somewhat because of the central limit theorem without significantly reducing the accuracy of these expressions, provided N is large (ref. 17). (This theorem states that the population of sample means from a nonnormal population approximates the normal distribution as N becomes large.) The coefficient Z_c controls the level of confidence associated with the interval. A 95% confidence level can be computed by choosing Z_c equal to 1.96. The mean estimator can then be expected to fall inside the bounds of the predicted uncertainty interval in about 95 out of each 100 data sets (N velocity values in each data set).

S_u and N are both known when data are acquired using standard counting techniques, and computation of Δu and ΔS is straightforward. When photon correlation techniques are used, the computation is more difficult because the value N is not measured directly by the correlator. An estimate of N can be made, however, based on the seed particle concentration, flow velocity, and data-acquisition times in order to estimate the uncertainties.

Combined Uncertainty—Counter Processor Measurement

In order to calculate a total uncertainty interval Δu for the mean velocity, it is necessary to estimate S_u based on combined statistical and systematic uncertainties. A method to combine uncertainties of these types is presented by Baird in reference 20. The combined estimator of the standard deviation of the u-velocity distribution is calculated (ref. 20) by using the expression

$$S_u = \left[\left(\frac{\partial u}{\partial f} \right)^2 S_f^2 + \left(\frac{\partial u}{\partial R} \right)^2 S_R^2 + \left(\frac{\partial u}{\partial B} \right)^2 S_B^2 \right]^{1/2}$$

The partial derivatives are obtained from equation (1), assuming small angles to simplify the expressions, and the value S_f is obtained directly from the ensemble average of frequency measurements. During the measurement of R and B, absolute uncertainty intervals DR and DB are estimated. These are converted to S_R and S_B using the method suggested by Baird. (The intervals DR and DB are chosen to bracket the actual value with about 100% certainty. They must be converted to intervals for which a 68% probability exists of bracketing the actual value. Since the DR and DB probability distributions are rectangular, two-thirds of the area under their probability distribution curves is enclosed by an interval two-thirds as large as the total absolute interval. S_R and S_B may therefore be approximated by 2/3(DR) and 2/3(DB), respectively.) The expression for S_u reduces to

$$\frac{S_u}{u} = \left[\left(\frac{S_f}{f} \right)^2 + \left(\frac{2\Delta R}{3R} \right)^2 + \left(\frac{2\Delta B}{3B} \right)^2 \right]^{1/2}$$

and the uncertainty Du/u is calculated by substituting S_u/u into equation (13). A 95% confidence interval about the mean of ±1.9% is typical for the mid-zoom range of 6.3 m.

Combined Uncertainty—Photon Correlation Measurement

The combined uncertainty associated with photon correlation mean velocity measurements can be expressed entirely in terms of absolute uncertainty intervals because no ensemble of discrete frequency measurements is made to obtain the velocity distribution. Instead, a single frequency measurement is made using a Fourier transformation to obtain the mean frequency of the correlogram. The uncertainty of this frequency is expressed as an absolute uncertainty interval using equation (12). Substitution

of typical values in equation (11) yields the absolute uncertainty interval about the mean, Δu, of $0.54 + 0.013u$ m/sec.

EXPERIMENTAL RESULTS

Experimental measurements were made in the controlled environment of the laboratory and in the more demanding environment of the wind tunnel to study the performance of the instrument. In the laboratory, a test flow field was generated at the measuring volume using a low-speed jet assembly especially constructed for laboratory testing. The jet, shown in figure 11, was powered by a 1.5-hp centrifugal blower. The rectangular exit of the blower was connected to the circular cross section of the exit nozzle by the transition duct shown. Nine screens positioned between the transition section and contraction nozzle, spaced at 1.3-cm intervals, dampened the turbulence and unsteadiness caused by the blower. The nominal velocity at the 10.0-cm diameter jet exit was 30 m/sec. In the wind tunnel, measurements were made in the test section flow field of the NFAC 80- by 120-Foot Wind Tunnel during the facility flow calibration test. A diagram of the test section showing the location of the instrument is presented in figure 12. The downstream location was selected to prevent interference with the primary flow calibration measurements being made at the instrumentation boom.

Low-Speed Jet Measurements

Velocity and turbulence-intensity profiles were acquired in the laboratory jet flow at two and four diameters from the jet exit. Measurement locations were spaced equally at 6.4-mm intervals along survey lines passing through the center of the jet. LV data were acquired twice during two separate surveys. The first survey was conducted using counter processors for data acquisition at a measurement range of 6 m. The second survey was performed using photon correlation at a 15-m range. Surveys at these same locations were also obtained using an X-wire two-element hot-wire probe.

LRLV data were taken under the following conditions. With the counter processors, 250 samples were acquired, at 16 cycles/sample. The average data rate was 40 to 60 samples/sec. With the photon correlator, a 2-min acquisition interval was selected with a delay increment of 15 nsec. Laser power was adjusted to 3 W in the former case and to 8 W in the latter. The flow was seeded to acquire the LV measurements using a dry diatomite seed material of nominal 3-mm particle size. The seed material was injected at the blower inlet and into the ambient air around the nozzle exit.

Hot-wire data were acquired at each survey location with an X-wire probe and computer data-acquisition system. The probe wires were 5-mm-diameter, platinum-coated tungsten with an active length of 1.25 mm. Direct digitization of the analog, nonlinearized anemometer outputs in real time was performed over 12-sec data-acquisition intervals at each location (1024 samples/wire). A square-law linearization was then computed during data reduction with a conversion to engineering units. Velocity and angle calibrations were performed immediately prior to conducting the surveys, to minimize drift.

Detailed profiles of axial and radial mean velocity and associated turbulence intensity, taken with the hot-wire anemometer at the two- and four-diameter survey locations from the jet exit, are presented in

figures 13(a) and 13(b), respectively. In figures 14 and 15, these data are presented as solid lines by connecting the data points with straight-line segments for comparison with the laser data. Figures 14(a) and 14(b) show the LV measurements of axial and radial mean velocity and turbulence intensity acquired at the two survey locations with the counter processor. Figures 15(a) and 15(b) show the same measurements acquired using the photon correlator.

Excellent agreement between hot-wire mean-velocity measurements and mean LV counter-based measurements is evident in Figures 14(a) and 14(b). Agreement between the turbulence-intensity measurements is also good. The LV data scatter is minimal, and the shape and magnitude of the turbulence-intensity profiles is, in general, accurately represented. The only significant deviations occur in the radial turbulence intensity profiles, where the LV measures a somewhat broader profile than the hot wire does.

The photon correlation LV data, figures 15(a) and 15(b), are more scattered than the counter-based measurements discussed earlier. Nevertheless, the mean axial profiles are in good agreement. The radial mean profiles differ somewhat, however. This difference could possibly have been caused by a slight misalignment of the jet centerline with respect to the LV beams combined with the ambient air currents that were present in the area of the measurement. The turbulence-intensity profiles, although also scattered, follow the basic profile shape of the hot-wire data.

Shown in figure 16 is a typical modified autocorrelation function and its associated cosine transformation. This distribution gives the velocity probability density (in terms of frequency in this case) as discussed earlier. The data point was taken during the survey of figure 15(b) and is labeled "A" in that figure. Also plotted in figure 16 is a Gaussian distribution with a standard deviation equal to that computed from the velocity probability density. The two distributions agree, indicating that the velocity probability density is Gaussian in nature.

Wind Tunnel Boundary-Layer Measurements

Velocity and turbulence-intensity profiles were acquired during the Facility flow calibration in the floor boundary layer of the 80- by 120-Foot Wind Tunnel, along a survey line located 9.5 m downstream of the model-support turntable center of rotation. The relative position of the LRLV in the test section is shown in figure 12. At this streamwise location, measurements were taken at the test section centerline and at a position 6.1 m from the centerline (to the right, looking upstream). The corresponding measurement ranges of these two positions were 6.3 and 13 m, respectively.

The LV measurements were taken using both the counter-based and photon correlation methods of data acquisition and reduction. Measurements were also taken with a total pressure rake for comparison to the LV data.

Initially, attempts were made to acquire LV data relying only on the natural seeding present in the flow. It was concluded that a significant concentration of natural seed particles collected in the open-circuit wind-tunnel inlet during periods when the tunnel was idle. This concentration of particles would pass through the test section at start-up during the first minute of operation. High-quality signals and large data rates were observed during this short period. The seed concentration would then drop to near

zero levels, at least in the size range required, at steady-state conditions, thereby reducing the LRLV data rate to nearly zero.

Injection of artificial seed particles at the wind tunnel inlet resulted in a substantial increase in data rate relative to the unseeded case. The seed material was injected into the flow using a rectangular array (1.2 m by 1.5 m) of 30 spray nozzles. The seed material, 3-μm-nominal-size diatomite particles, was carried in a 1:1 solution of water and ethyl alcohol. The solution was contained in a 57-liter holding tank and was continuously agitated by a recirculation pump. Approximately 2 cc of diatomite (loose density 128 kg/m^3) was used per liter of solution. This mixture was injected at a rate of about 1.0 liters/min.

The spray nozzle array was located at the wind tunnel inlet as shown in figure 17. Its position was carefully selected to generate a stream tube containing the seed material that would pass through the measurement area in the test section. The location of the stream tube was verified visually using a smoke generator. Smoke was released at the inlet spray-nozzle array location and observed in the test section, and the array was repositioned as required.

LV data were taken using counter-based and photon correlation acquisition and processing techniques. Two hundred and fifty samples were taken at each point with the counters, at data rates in the range of 40-60 samples/sec. An acquisition period of 2 min was selected with the photon correlator, using 25 nsec as the delay increment. Both methods required a laser power of 8 W.

Presented in figure 18(a) are the measured boundary-layer profiles of the horizontal component of mean velocity and the associated component of turbulence intensity. Counter, photon correlator, and rake mean measurements are plotted in the figure for comparison. The agreement between the three measurements is generally good. The associated LV turbulence-intensity measurements are also in fairly good agreement, but do show some difference. One possible reason for this difference is that the counter data were taken at the centerline, whereas the photon correlation data were taken 6.1 m from this location. Additionally, external ambient wind conditions outside the wind tunnel inlet varied from run to run and could conceivably account for some differences.

Figure 18(b) shows the mean velocity and turbulence intensity profiles of the component perpendicular to the floor of the wind tunnel. Only counter measurements of this component are presented. Wind tunnel schedule constraints prevented the acquisition of the photon correlation data for this velocity component. The available data are presented here for completeness and possible future comparison.

CONCLUDING REMARKS

The LV performed well in the wind tunnel environment. Artificial seeding was required to obtain sustained data rates at acceptable levels. A concern prior to testing was whether the optical alignment would remain stable when the instrument was subjected to the wind tunnel flow. During testing in the 80- by 120-Foot Wind Tunnel, the alignment was found to remain stable, requiring only occasional minor adjustment. In general, performance and accuracy were found to meet or exceed expectations.

Future work will focus on improving the accuracy of the measurements made using the photon correlation acquisition and reduction technique, and on the development of a more versatile method for artificially seeding the facilities of the NFAC.

APPENDIX

CORRECTION OF TURBULENCE

A data-reduction technique is described in the preceding sections which uses a discrete Fourier cosine transformation to extract turbulence information from measured autocorrelation data. The finite length of the autocorrelation record causes a truncation effect that broadens the velocity probability distribution recovered by the technique, however, and an error is introduced when turbulence is predicted using this distribution. The method suggested by Abbiss in reference 4 for correction of the error is applied in this appendix to develop the look-up table necessary for correction of the turbulence.

Approach

A statistical model is developed which numerically simulates the correlation process by generating an autocorrelation function having the proper shape for a given level of turbulence. By reducing this autocorrelation function using the cosine transformation technique for different levels of turbulence, a table of corresponding apparent values is obtained. The look-up table is constructed using these values.

Model

The autocorrelation function is numerically calculated using the following set of equations (ref. 21):

$$R_{nn}(k\tau) = \sum_{i=1}^{T/\tau} n_i n_{i+k} \qquad k = 1, 2, 3, 4, \cdots, K \tag{A1}$$

where

T = total time of data collection
k = index for delay increment
n_i = number of photon pulses detected in the ith delay cycle
K = total number of autocorrelation coefficients (256)

Each value n_i represents the number of photon pulses detected in the ith delay cycle. Some of these photons arrive at random intervals and contribute only to the uniform background level of the autocorrelation function. Others are scattered at the measuring volume when a particle traverses it. These are correlated in time and contribute to the periodic shape of the autocorrelation function, but not all are detected at the photocathode. The likelihood of detection is governed by a probability distribution, the shape of which is shown in figure A1, assuming a Gaussian beam-intensity profile. The distribution changes slightly with each particle transit owing to the different particle sizes, velocities, and trajectories through the measuring volume. For a given particle transit, the probability is expressed by the equation (ref. 22)

$$P_b(i) = \frac{P_{bm}}{2}[\cos(2\pi fi) + 1]\mathrm{EXP}\left[-\frac{4i^2}{\left(\frac{2r_o}{u\cos(\beta/2)}\right)^2}\right] \qquad \text{(A2)}$$

where

$P_b(i)$ = probability of photon detection during ith delay cycle
P_{bm} = peak probability at center of burst
i = delay cycle counter
f = Doppler frequency including offset frequency f_o
r_o = radius of beam waist (1/e)
u = particle velocity corresponding to Doppler frequency $(f - f_o)$
$\frac{2r_o}{u\cos(\beta/2)}$ = particle passage time through measuring volume

A flow chart giving the major steps in the calculation is shown in figure A2. The constant terms which are input or calculated at the beginning are time delay increment, fringe spacing, shift frequency, and fringe velocity. A Gaussian velocity distribution is then randomly created having a given mean value and standard deviation. Each velocity element within the distribution array represents a simulated Doppler burst. Its value is used to calculate burst duration and Doppler period for each burst.

To model shorter bursts when particle transits do not pass exactly through the center of the measuring volume, a random component is subtracted from the burst duration. These parameters are then used to calculate the probability distribution of figure A1 using equation (A2), for each burst in the distribution, and the autocorrelation function is calculated with equation set (A1) using the probability at each delay time to determine the value n_i. A small random number of counts is then added to n_i at random time delays to model the background detections.

Plotted in figure A3 is the numerically generated autocorrelation function for 5.5% turbulence. Also plotted in the figure, for the same conditions, is an actual data point obtained in the 80- by 120-Foot Wind Tunnel. Agreement is equally good at other levels of turbulence.

Correction

The correction table is obtained by reducing autocorrelation functions generated using the statistical model with different initial inputs of turbulence and mean velocity. An apparent standard deviation is computed, which differs from the true value owing to truncation, using the cosine transformation technique described. When the specified, true standard deviation is plotted against the calculated, apparent standard deviation, as suggested in reference 4, the curve of figure A4 is obtained.

A polynomial is fit to the data points using least squares to make the correction easier. It is implemented using this polynomial to compute the true standard deviation for a given apparent value.

REFERENCES

1. Zell, P.; and Flack, K.: Performance and Test Section Flow characteristics of the National Full-Scale Aerodynamics Complex 40- by 80-Foot Wind Tunnel. NASA TM-101065, 1988.

2. Reinath, M. S.; Orloff, K. L.; and Snyder, P. K.: A Laser Velocimeter System For Large-Scale Aerodynamic Testing. NASA TM-84393, 1984.

3. Reinath, M. S.; and Ross, J. C.: Prediction of the Flow-Field Interference Induced by the Long-Range Laser Velocimeter in the Ames 40- by 80-Foot and the 80- by 120-Foot Wind Tunnels. NASA TM-86763, 1985.

4. Abbiss, J. B.: The Structure of the Doppler-Difference Signal and the Analysis of its Autocorrelation Function. Physica Scripta, vol. 19, no. 4, 1979, pp. 388-395.

5. Abbiss, J. B.: Theoretical Aspects of Photon Correlation Methods in Doppler-Difference Anemometry. Proc. 4th Intern. Conf. Photon Correlation Techniques in Fluid Mechanics, Stanford Univ., CA, 25-27 August 1980.

6. Abbiss, J. B.: Photon Correlation Velocimetry in Aerodynamics. In Photon Correlation Spectroscopy and Velocimetry, H. Z. Cummins and E. R. Pike, eds., Plenum Press, 1977, pp. 386-424.

7. Abbiss, J. B.; Bradbury, L. J. S.; and Wright, M. P.: Measurements on an Axi-Symmetric Jet Using a Photon Correlator. Proc. LDA-Symposium, Copenhagen, 1975, pp. 319-335.

8. Moore, C. J.; and Smart, A. E.: Retrieval of Flow Statistics Derived From Laser Anemometry by Photon Correlation. J. Phys. E: Sci. Instrum., vol. 9, 1976, pp. 977-981.

9. McWhirter, J. G.; and Pike, E. R.: The Extraction of Information from Laser Anemometry Data. Physica Scripta, vol. 19, 1979, pp. 417-425.

10. Sharpe, P. R.: An On-Line Data Reduction System for Photon Correlation Laser Anemometry. Physica Scripta, vol. 19, 1979, pp. 411-416.

11. Brigham, E. O.: The Fast Fourier Transform. Prentice-Hall, Inc., 1974.

12. Durst, F.; Howe, B.; and Richter, G.: Long-Range LDA Wind Velocity Measurements Using Visible Laser Radiation. Proc. 4th Intern. Conf. Photon Correlation Techniques in Fluid Mechanics, Stanford Univ., CA, 25-27 August 1980.

13. Durst, F.; and Richter, G.: Neuere Entwicklungen auf dem Gebiet der Laser-Doppeler-Windgeschwindiskeitsmessungen Teil II: Meßsystem fuer Freilandmessungen und sein Einsatz. Zeitschrift Fuer Flugwissenschaften und Weltraumforschung, vol. 7, 1983, pp. 263-273.

14. Orloff, K. L.; and Snyder, P. K.: Laser Doppler Anemometer Measurements Using Nonorthogonal Velocity Components: Error Estimates. Appl. Opt., vol. 21, 1982, pp. 339-344.

15. Durst, F.; Melling, A.; and Whitelaw, J. H.: Principles and Practice of Laser-Doppler Anemometry. Academic Press, Inc., 1976.

16. Miller, I.; and Freund, J. E.: Probability and Statistics for Engineers. Third Ed., Prentice-Hall, Inc., 1985.

17. Mack, C.: Essentials of Statistics for Scientists and Technologists. Plenum Press, 1967.

18. Freund, J. E.; Livermore, P. E.; and Miller, I.: Manual of Experimental Statistics. Prentice-Hall, Inc., 1960.

19. Spiegel, M. R.: Theory and Problems of Statistics. McGraw-Hill, 1961.

20. Baird, D. C.: Experimentation. Prentice Hall, 1988.

21. Mayo, W. T.; Woodward, R. P.; Boland, A.; and Smart, A. E.: Correlex: A Multiplexed Correlation Processor. Proc. 4th Intern. Conf. Photon Correlation Techniques in Fluid Mechanics, Stanford Univ., CA, 25-27 August 1980.

22. Durrani, T. S.; and Greated, C. A.: Laser Systems in Flow Measurement. Plenum Press, 1977.

TABLE I. – LONG RANGE LASER VELOCIMETER DESCRIPTIVE SPECIFICATION

	STANDARD FOCUS	EXTENDED FOCUS
GENERAL		
LASER HEAD	ARGON ION	ARGON ION
NOMINAL MAX POWER	1.8 W	18 W
WAVELENGTH	514.5 AND 488.0 nm	514.5 AND 488.0 nm
EXTERNAL DIMENSIONS		
LENGTH	3.90 m	3.90 m
WIDTH	0.75 m	0.75 m
HEIGHT	1.50 m	1.50 m
MASS	910 kg	910 kg
INPUT POWER	440 V, 3-PHASE w gnd, 38 kW	440 V, 3-PHASE w gnd, 38 kW
	110 V, 30 amps	110 V, 30 amps
COOLING WATER	0.22 liter/sec	0.22 liter/sec
BEAM GEOMETRY[a]		
FOCAL VOLUME SIZE		
LENGTH	10 mm	30 mm
DIAMETER	0.2 mm	0.4 mm
NUMBER OF FRINGES	15	15
GRINGE SPACING	12.7 μm	27.5 μm
BEAM SPACING (AT OUTPUT APERTURE)	25.5 cm	28.0 cm
BEAM CONVERGENCE ANGLE	2.3 deg	1.1 deg
POSITIONING RESOLUTION		
ZOOM POSITION	± 4 mm	± 4 mm
ROTATIONAL POSITION	± 0.06 deg (± 10 mm AT 10 m)[b]	± 0.06 deg (± 10 mm AT 10 m)[b]
LATERAL POSITION	± 4 mm	± 4 mm
WITH VIBRATION		
ZOOM POSITION	± 7 mm	± 7 mm
ROTATIONAL POSITION	± 0.09 deg (± 15 mm AT 10 m)[b]	± 0.09 deg (± 15 mm AT 10 m)[b]
LATERAL POSITION	± 7 mm	± 7 mm
OPTICAL CONFIGURATION		
TRANSMITTING LENSES	CUSTOM 3-MODULE ZOOM SYSTEM	CUSTOM 3-MODULE ZOOM SYSTEM
ZOOM FOCUS	2.6 TO 10 m	10 TO 20 m
RECEIVING METHOD	BACKSCATTER THROUGH TRANSMITTING LENSES AT STATIONARY PHOTOMULTIPLIER	BACKSCATTER THROUGH ISOLATED, STATIONARY, CO-AXIAL LENS AT TRANSLATING PHOTOMULTIPLIER
ACOUSTO-OPTIC SHIFTING	EACH OF 4 BEAMS	EACH OF 4 BEAMS
PERFORMANCE		
VELOCITY COMPONENTS MEASURED (WITH VERTICAL BEAM ORIENTATION)	AXIAL AND LATERAL RELATIVE TO TEST SECTION AXIS	AXIAL AND LATERAL RELATIVE TO TEST SECTION AXIS
VELOCITY RESOLUTION	1.9 % OF MEASURED VELOCITY	(0.54 ± 0.013 V) m/sec
TURBULENCE COMPONENTS MEASURED	NORMAL STRESS	NORMAL STRESS
THRESHOLD VALUE	1.5 % OF FREESTREAM	1.5 % OF FREESTREAM
DATA ACQUISITION TIME	1 min DEPENDING ON SEEDING DENSITY AND TURBULENCE	1 min DEPENDING ON SEEDING DENSITY AND TURBULENCE

[a]AT MID-ZOOM FOCAL DISTANCE [b]IMPROVED DESIGN IN PROGRESS

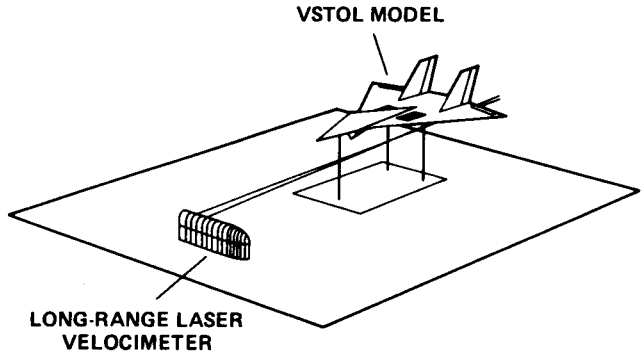

Figure 1.– Conceptual VSTOL aircraft hover test application of the LRLV at the NFAC Outdoor Aerodynamic Research Facility.

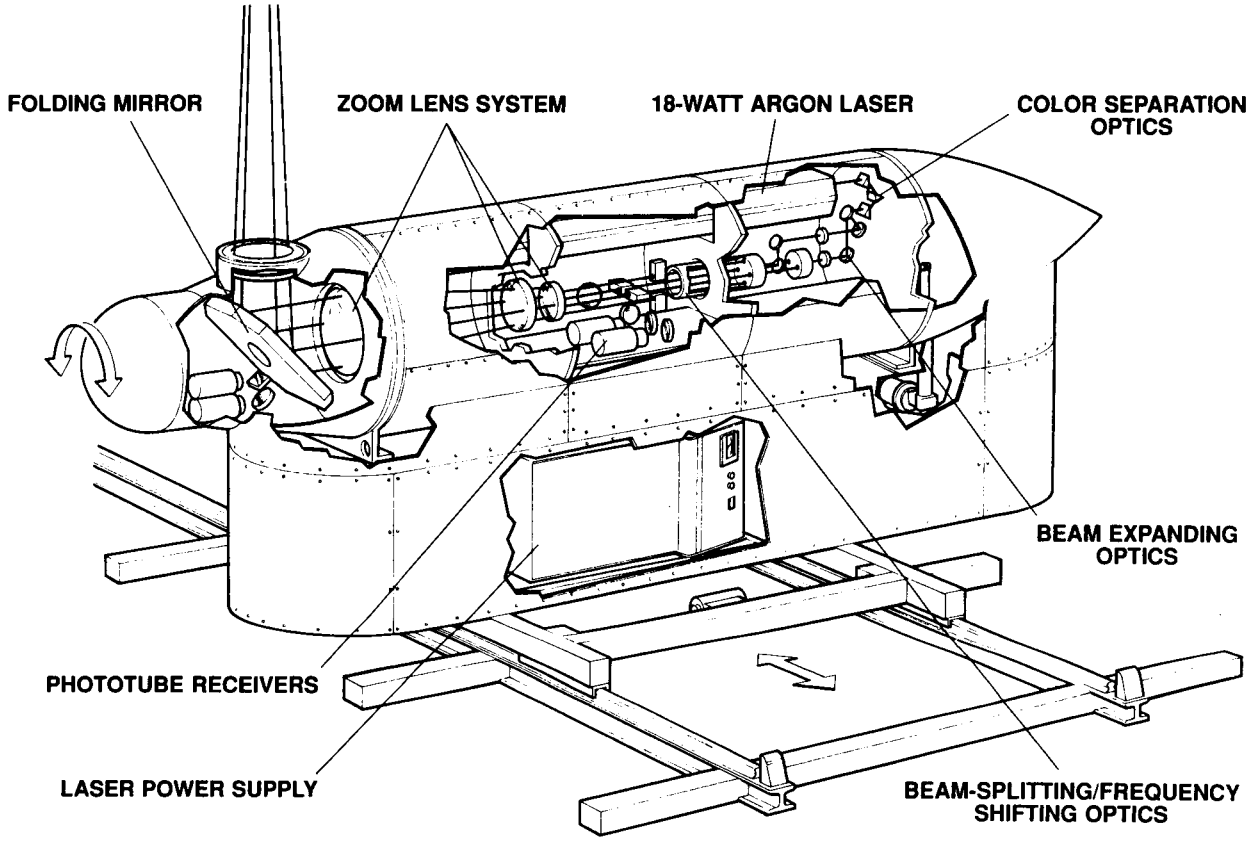

Figure 2.– Velocimeter system mounted on lateral traversing rails with portions of skin cut away to show major components.

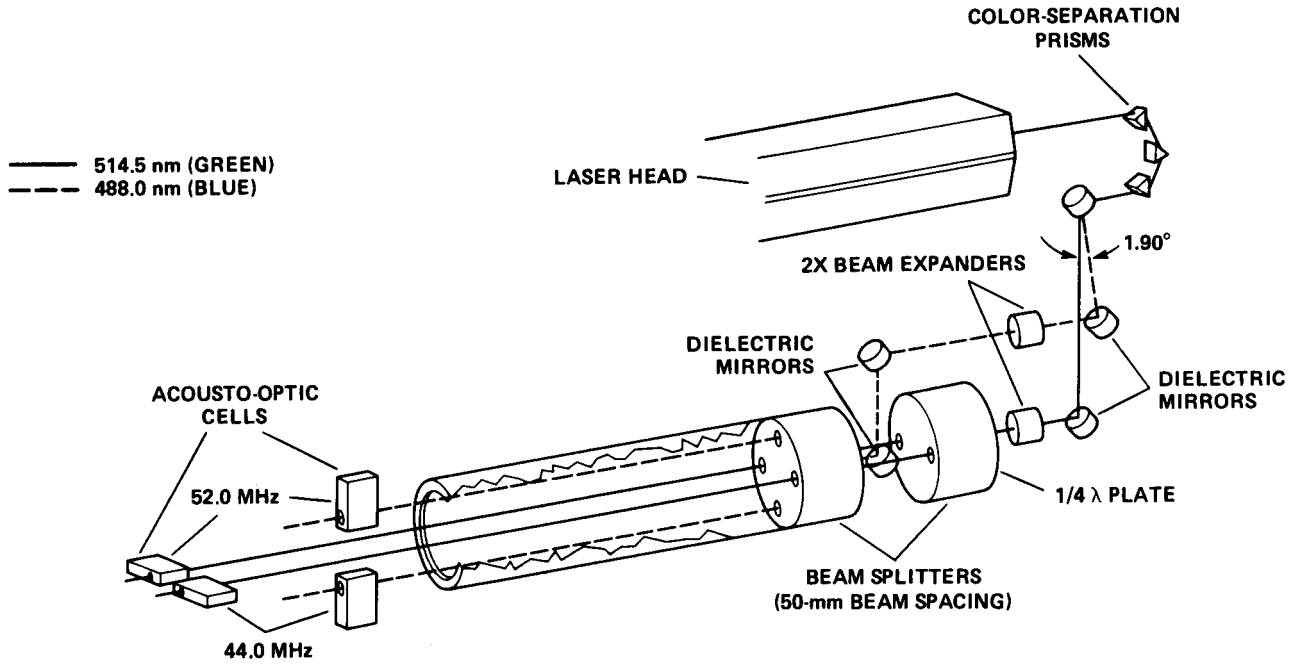

Figure 3.– Major elements of the transmitting optics (focusing lenses and folding mirror not shown).

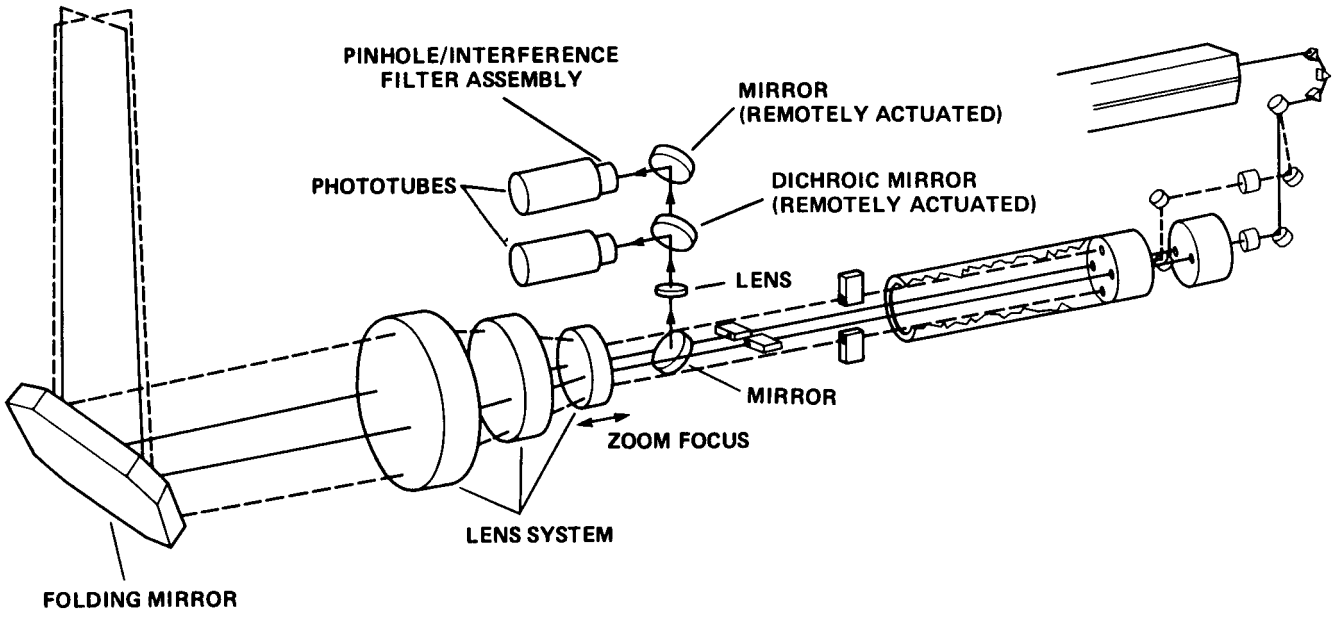

Figure 4.– Receiving optics for the 2.6- to 10-m focus range.

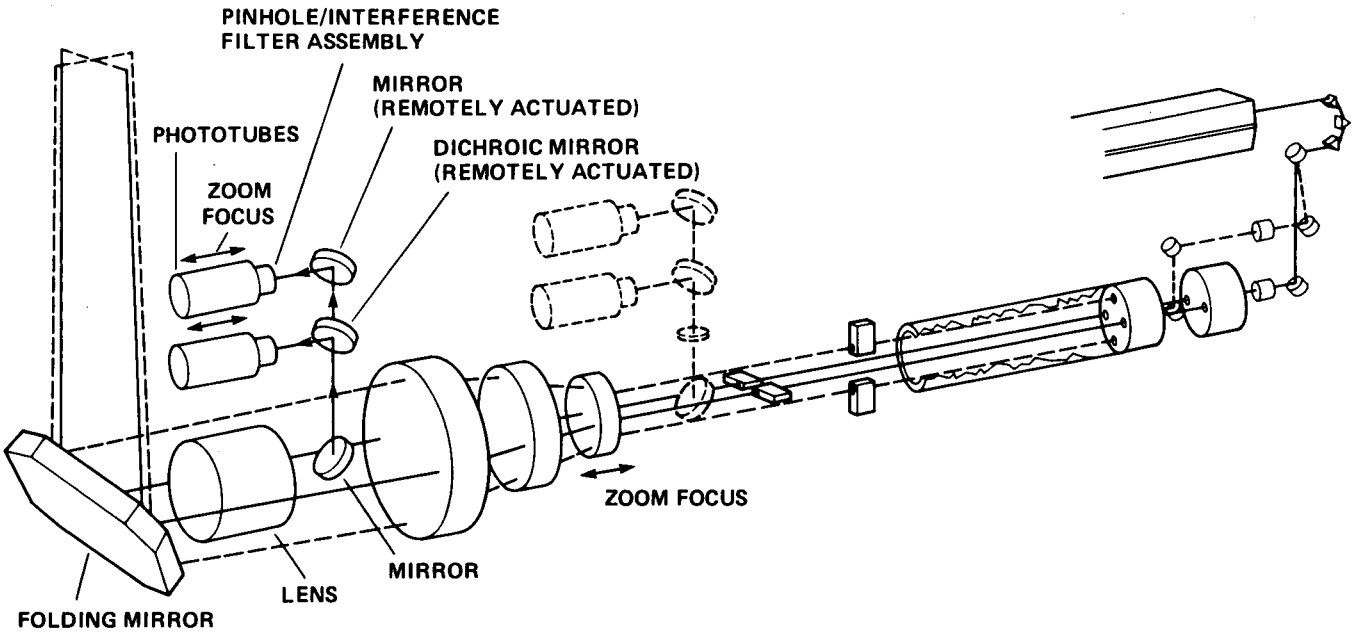

Figure 5.– Receiving optics for the 10- to 20-m focus range.

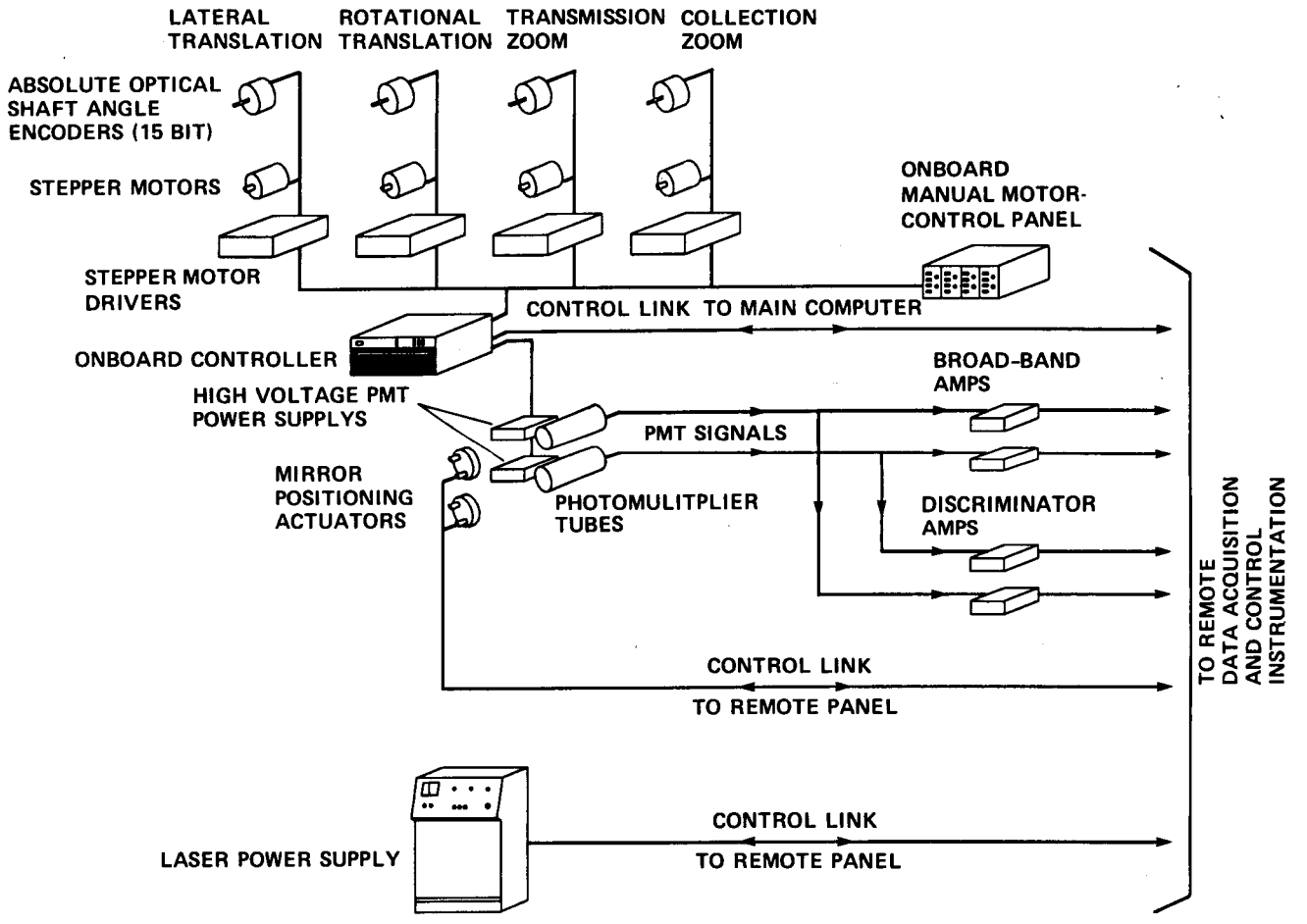

Figure 6.– On-board data acquisition and control instrumentation.

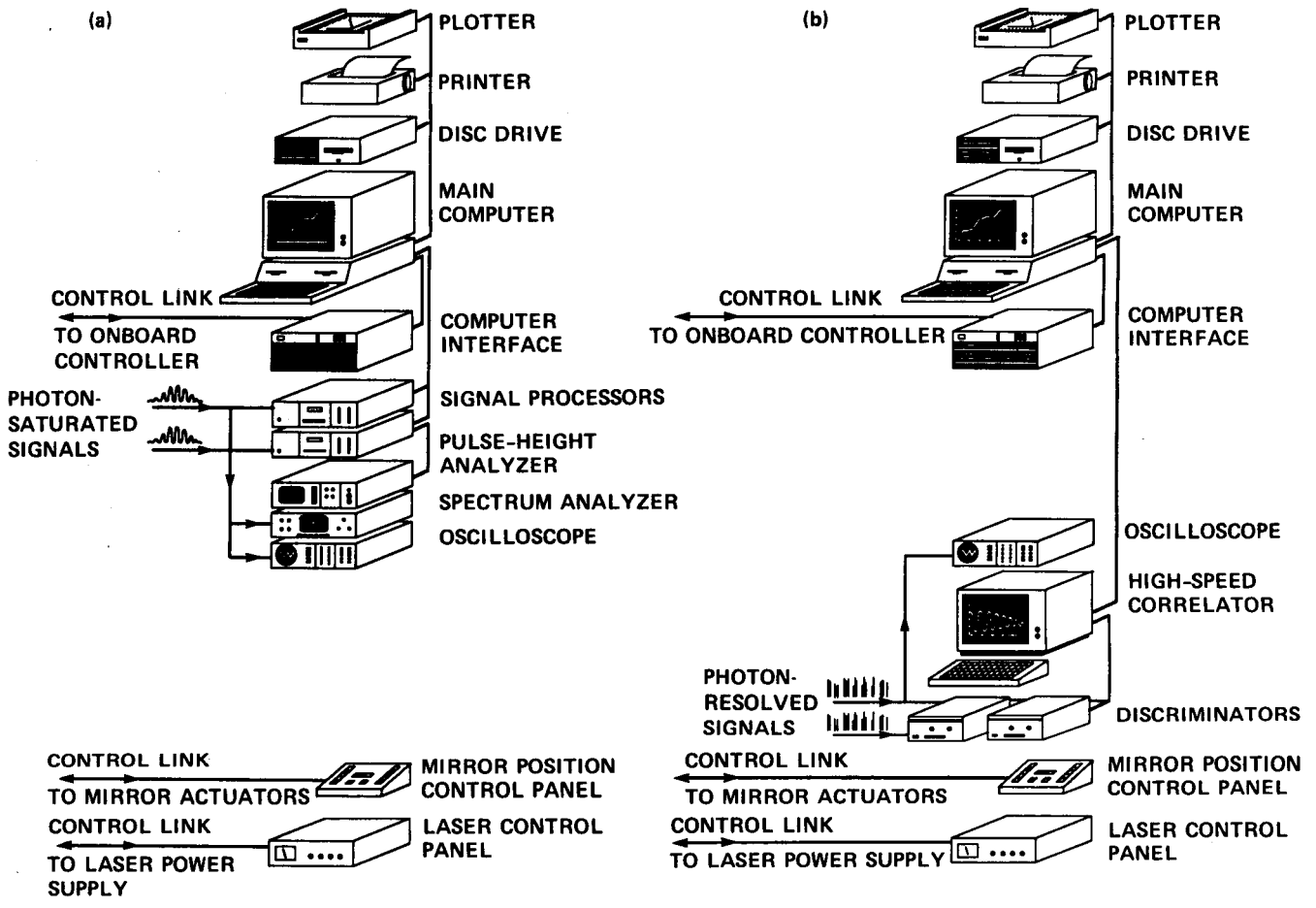

Figure 7.– Remote data-acquisition and control instrumentation used for acquiring and processing: (a) photon-saturated signals; (b) photon-resolved signals.

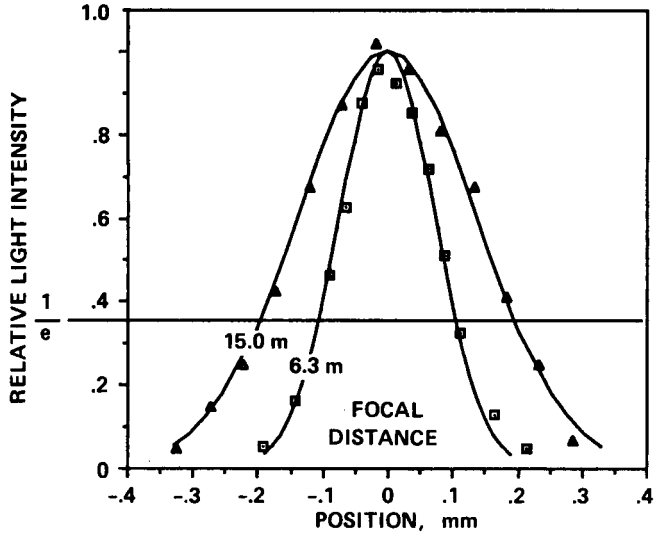

Figure 8.– Focal volume intensity profile through the center of the probe volume perpendicular to the optical axis (solid curves are the Gaussian fits to the measurements indicated by the symbols).

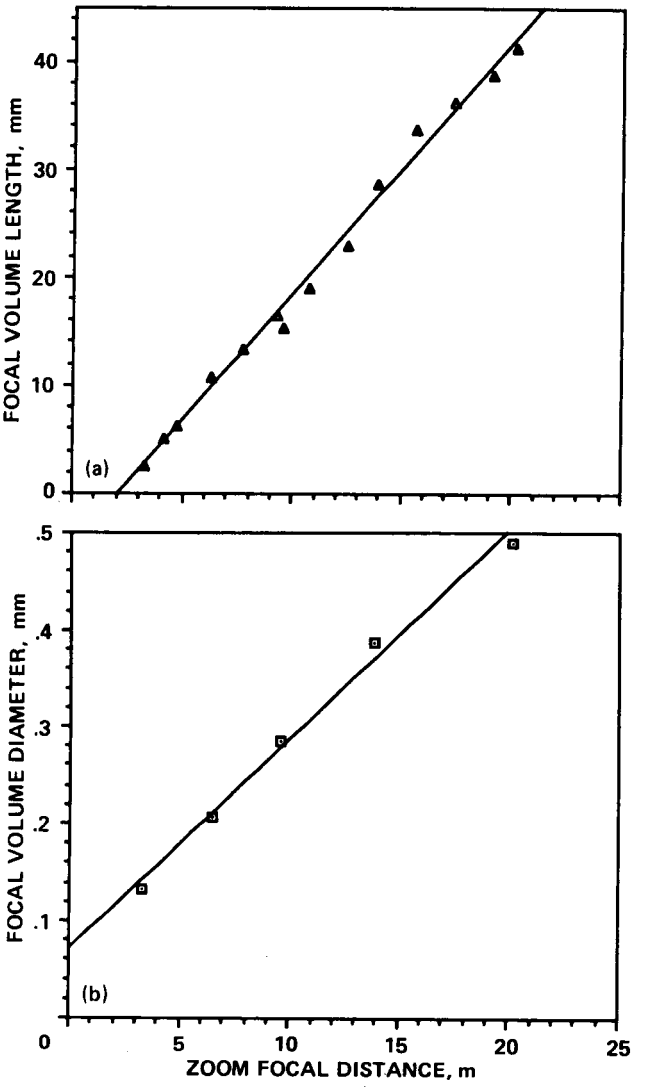

Figure 9.– Focal volume characteristics to the 1/e points plotted as a function of zoom focal distance: (a) focal volume length; (b) focal volume diameter.

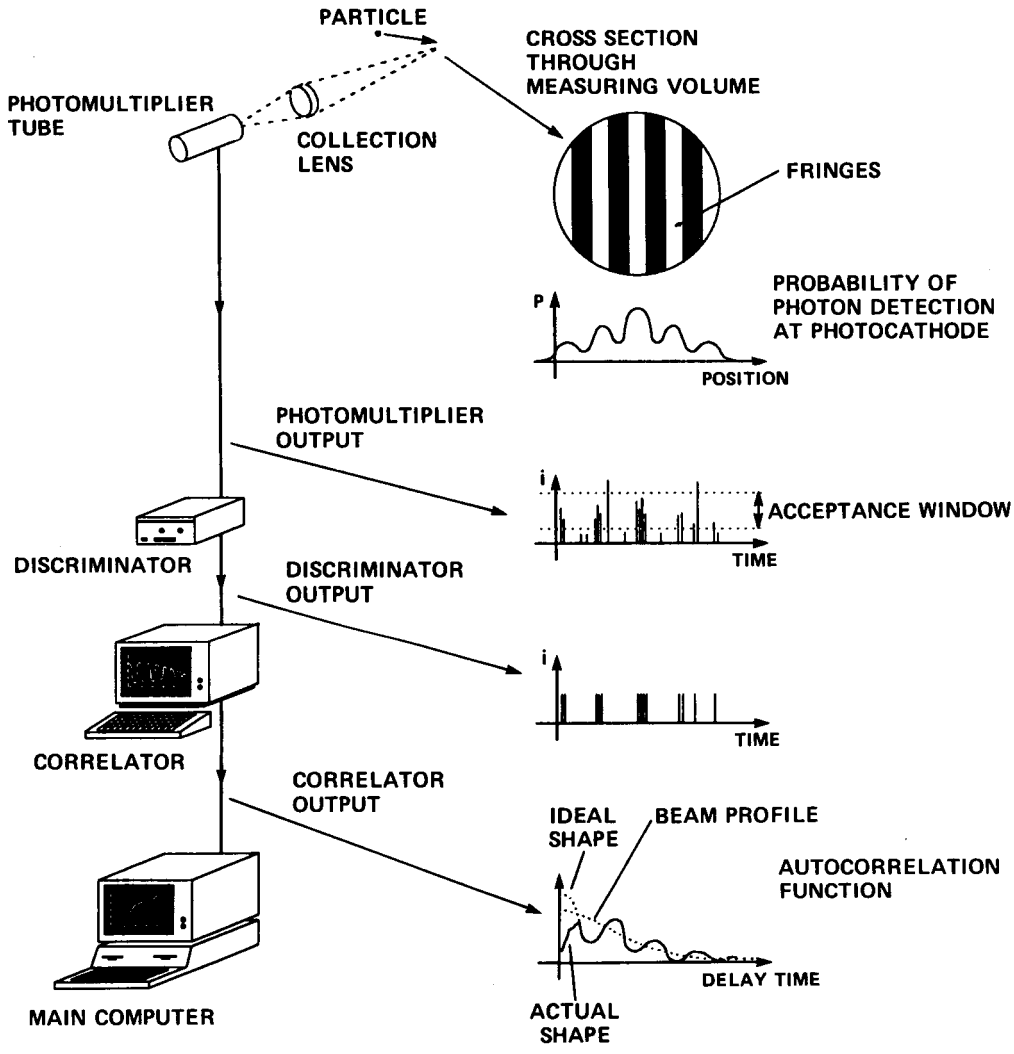

(a) Data acquisition.

Figure 10.– Overview of the data-acquisition and data-reduction process of photon-resolved signals.

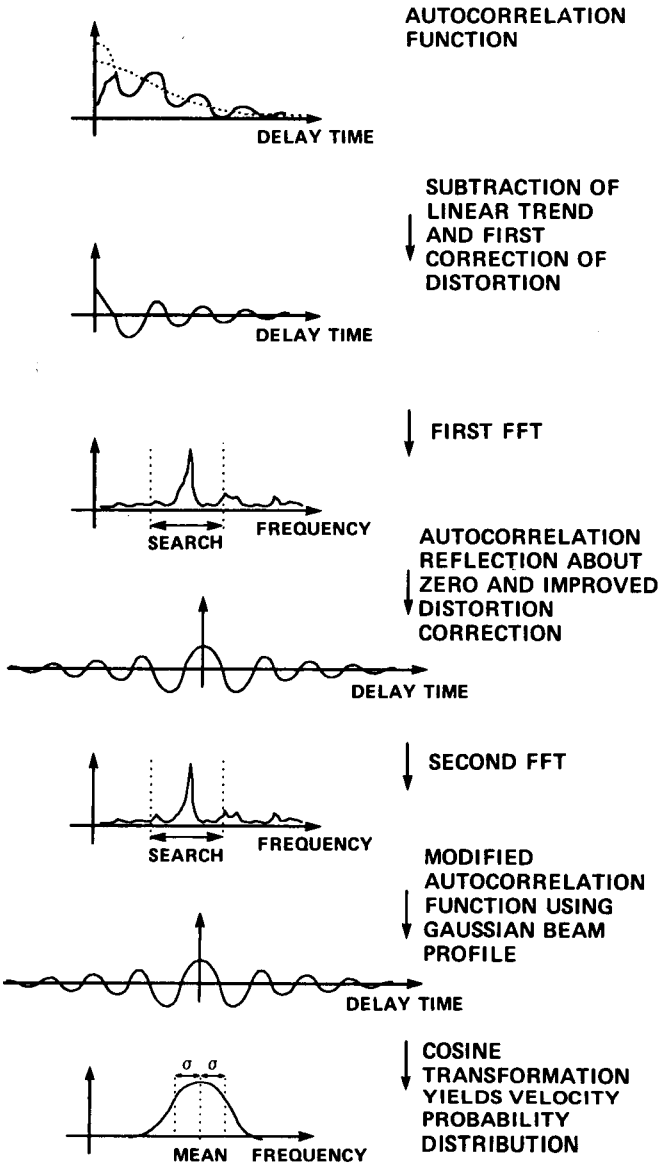

(b) Data reduction.

Figure 10.– Concluded.

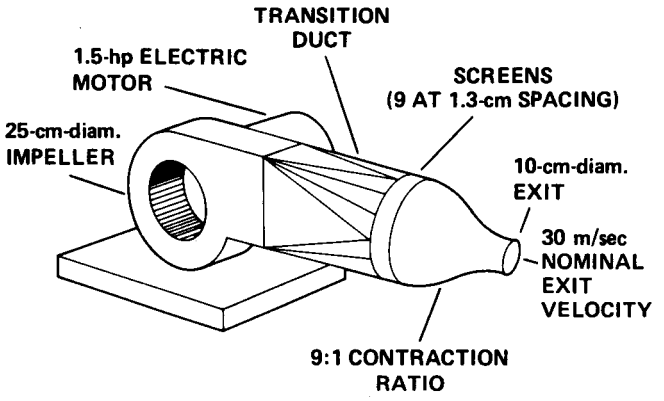

Figure 11.– Flow source used to generate low-speed jet for laboratory testing.

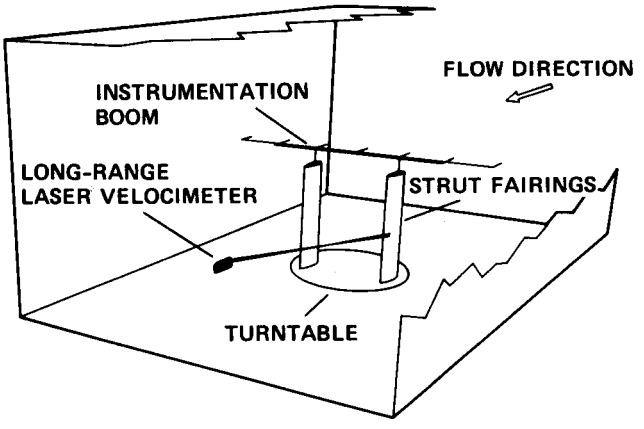

Figure 12.– LRLV shown to scale in the NFAC 80- by 120-Foot Wind Tunnel test section.

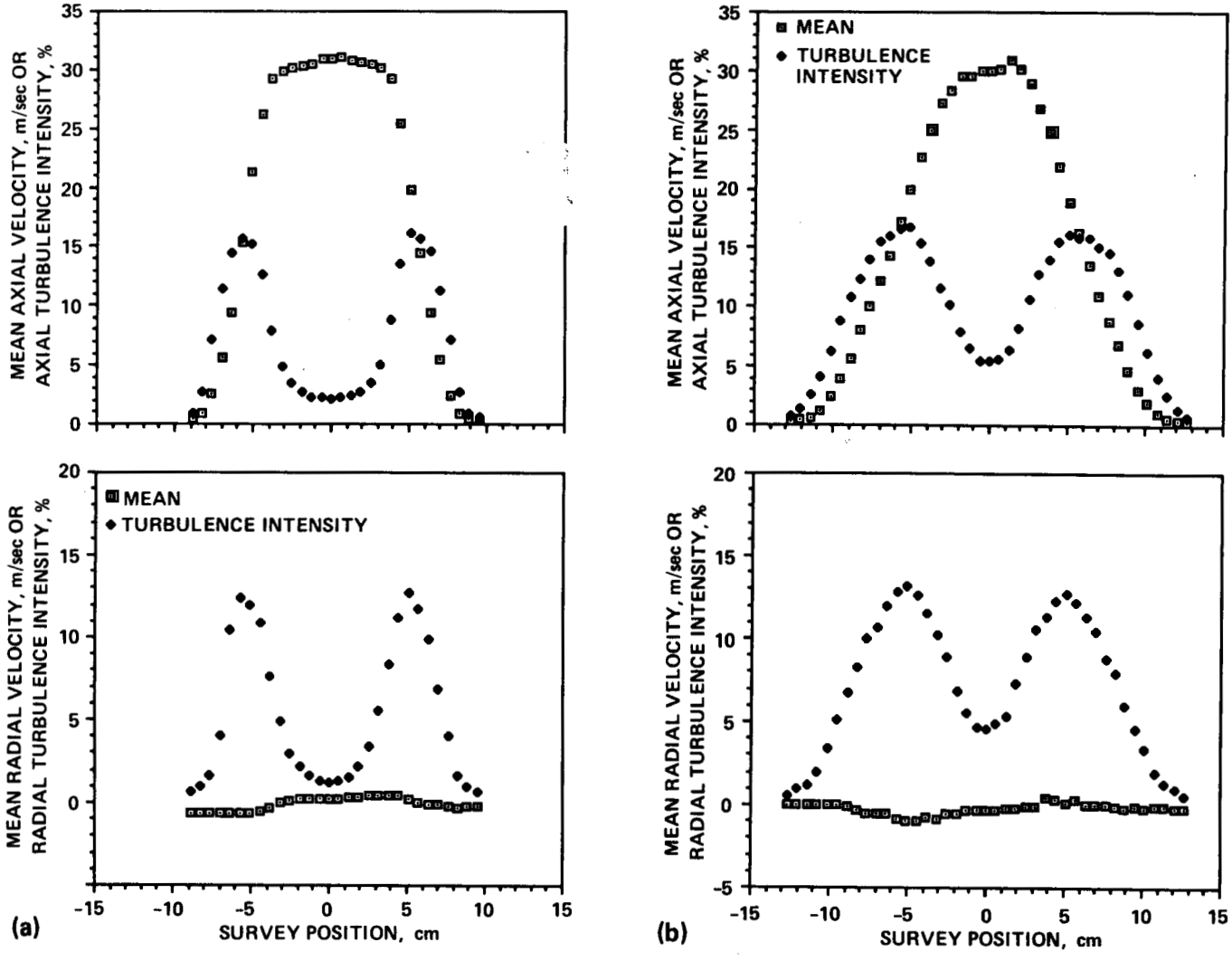

Figure 13.– Hot-wire measurement of axial and radial mean velocity and turbulence intensity: (a) two diameters from exit of jet; (b) four diameters from exit of jet.

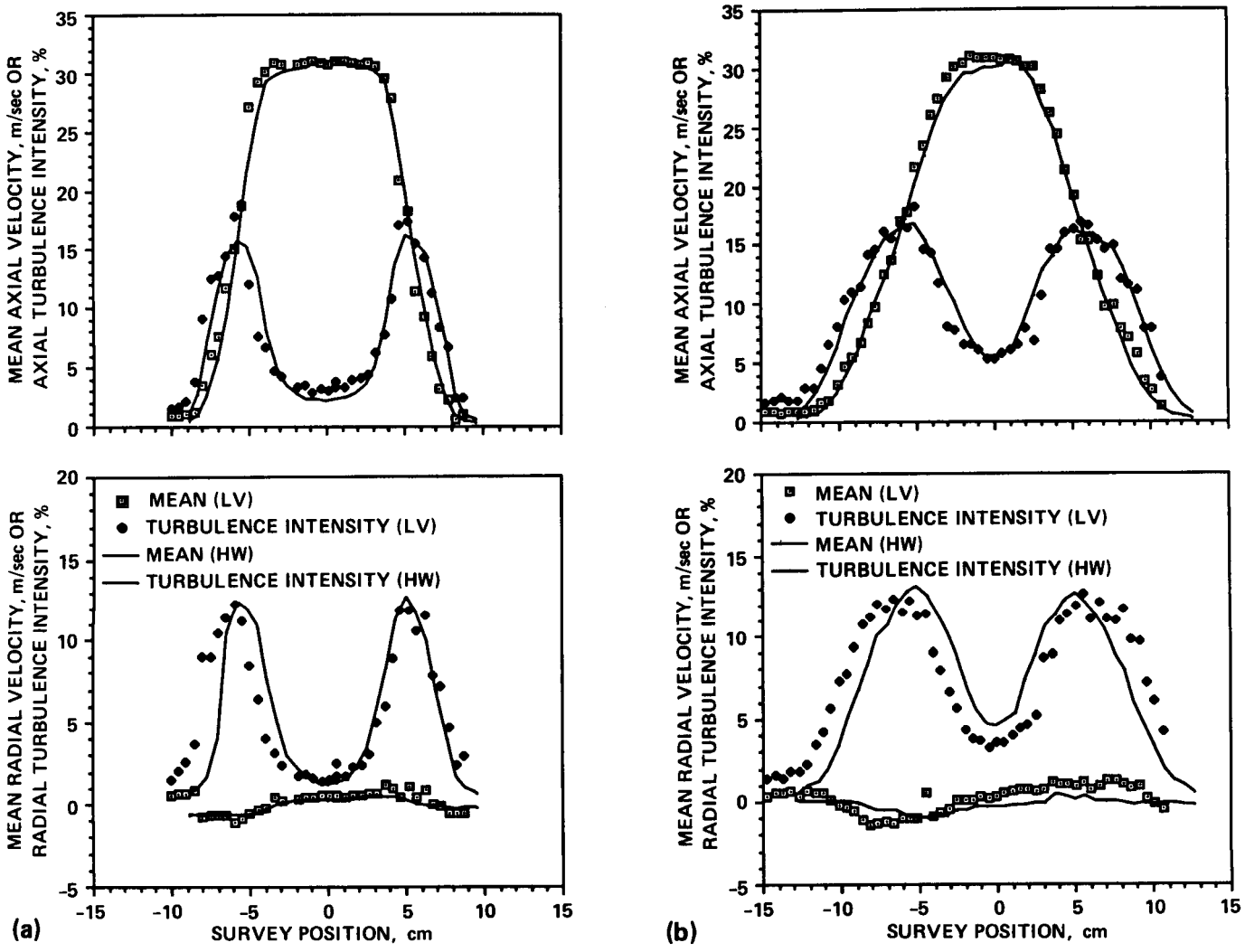

Figure 14.– LV counter-based measurement of axial and radial mean velocity and turbulence intensity (solid curves are hot-wire measurements of fig. 13 plotted for comparison): (a) two diameters from exit of jet; (b) four diameters from exit of jet.

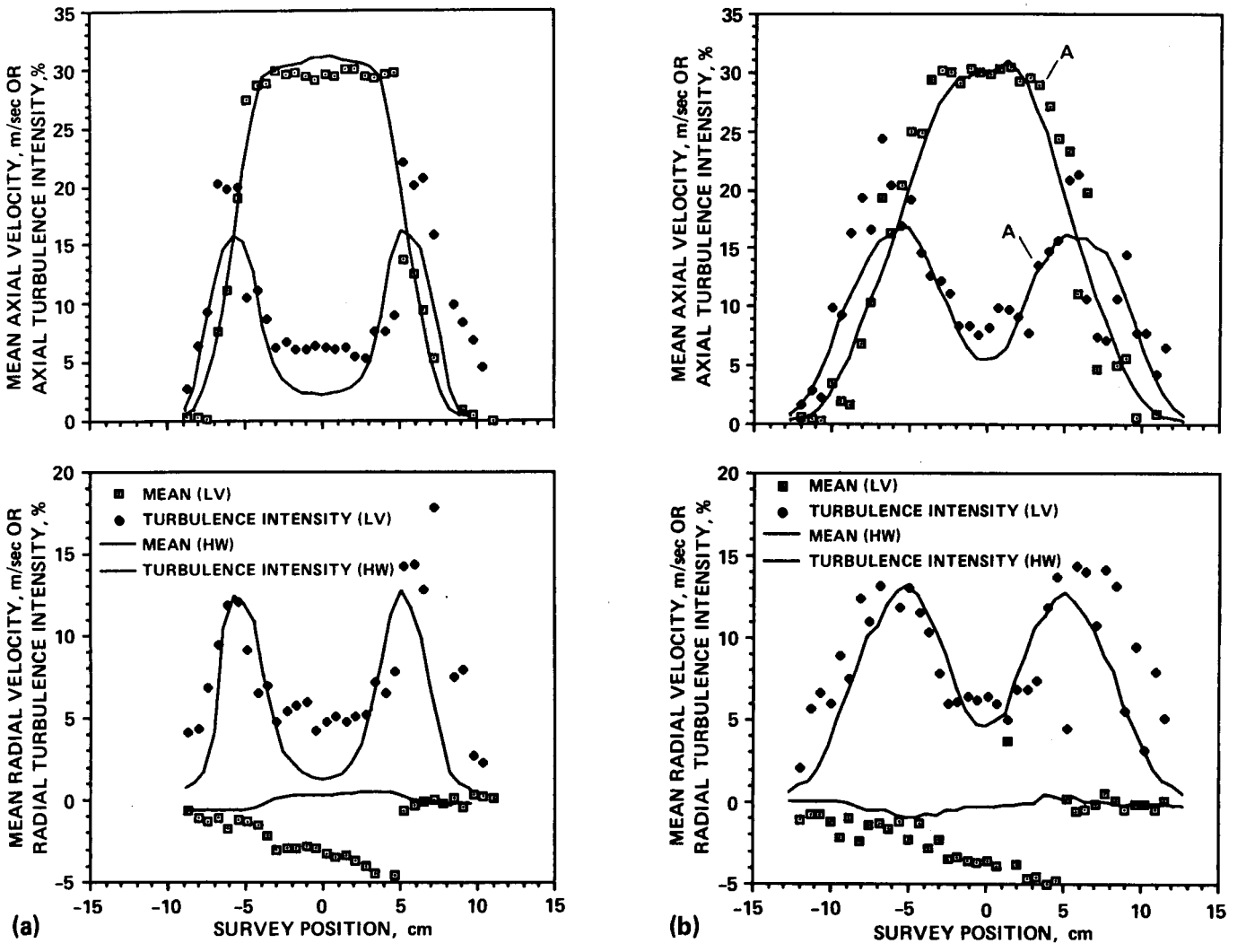

Figure 15.– LV photon-correlator-based measurement of axial and radial mean velocity and turbulence intensity (solid curves are hot-wire measurements of fig. 13 plotted for comparison): (a) two diameters from exit of jet; (b) four diameters from exit of jet.

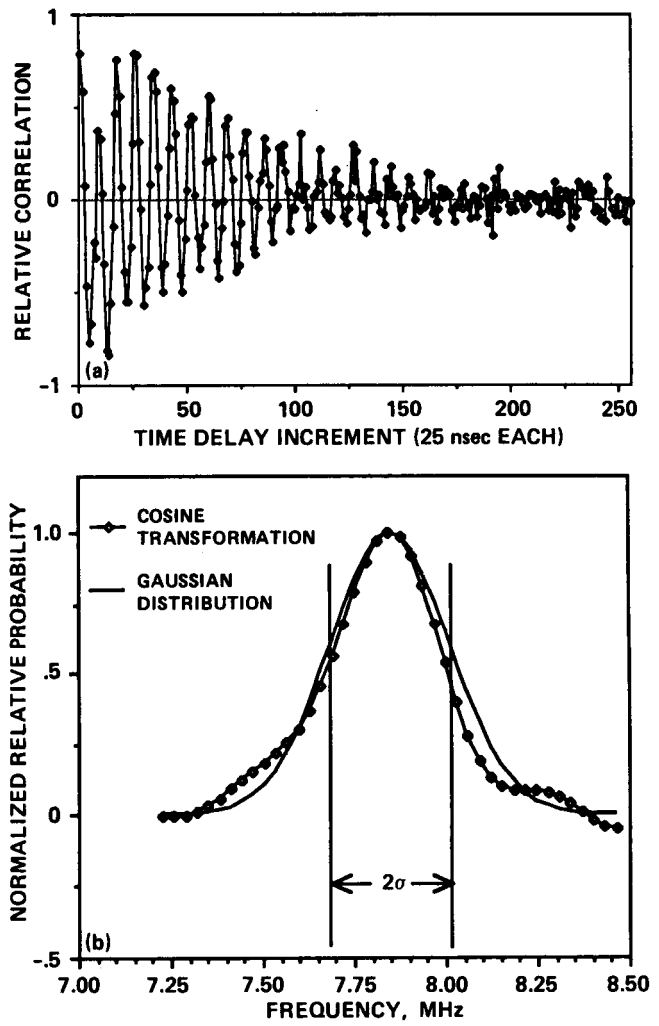

Figure 16.– Autocorrelation function and corresponding cosine transformation of the data point labeled "A" in figure 15(b): (a) modified autocorrelation function; (b) cosine transformation (also plotted is the Gaussian distribution having the same σ as the cosine transformation).

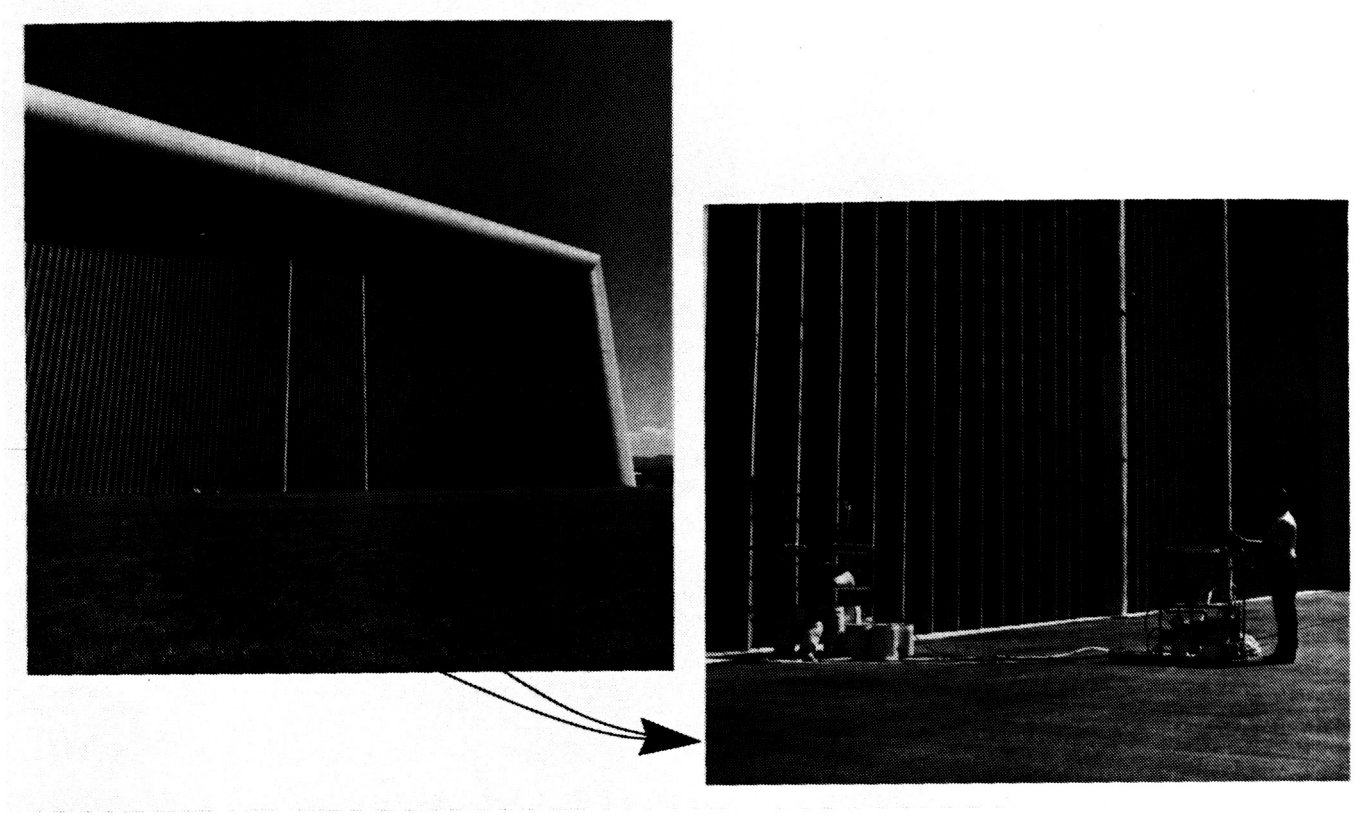

Figure 17.– Seeding apparatus at inlet of 80- by 120-Foot Wind Tunnel.

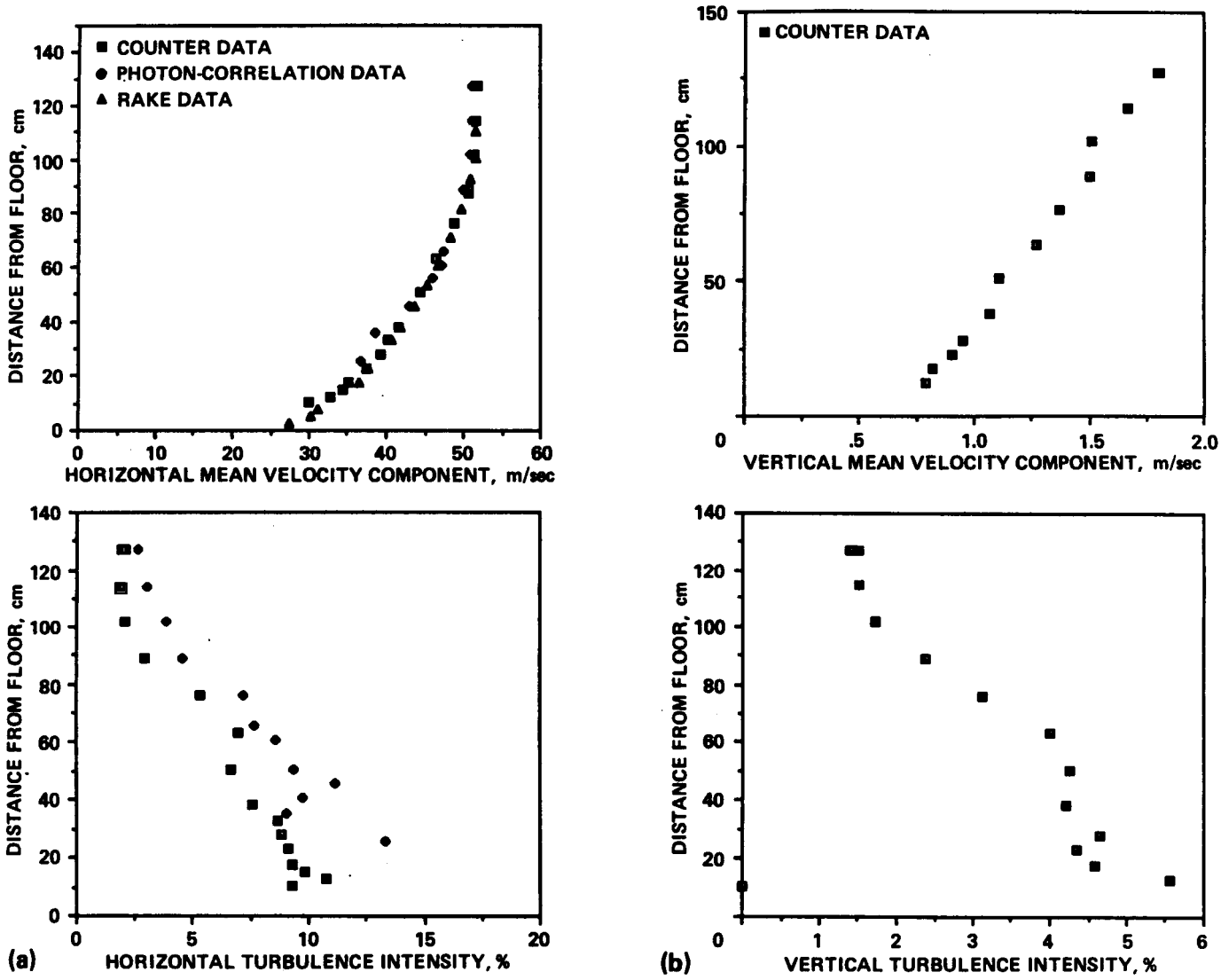

Figure 18.– Mean velocity and turbulence intensity profiles acquired in the boundary layer of the 80- by 120-Foot Wind Tunnel: (a) horizontal component; (b) vertical component.

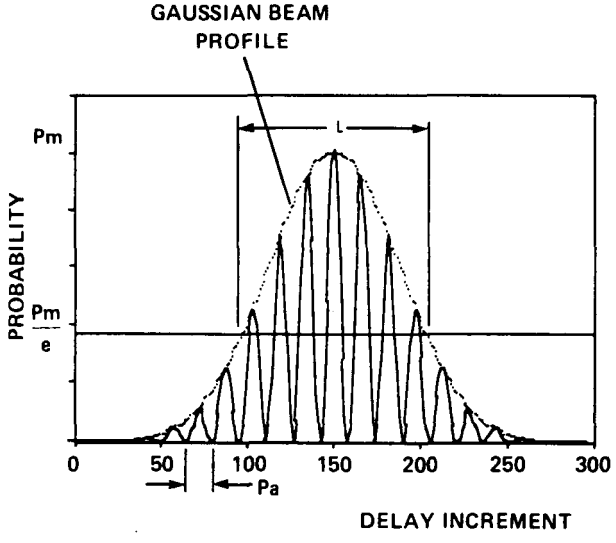

WHERE

Pm = MAXIMUM PROBABILITY OF DETECTION (VARIES WITH PARTICLE SIZE AND TRAJECTORY THROUGH THE MEASURING VOLUME)

Pa = FRINGE CROSSING PERIOD IN DELAY UNITS (VARIES WITH PARTICLE VELOCITY)

L = BURST DURATION IN DELAY UNITS (VARIES WITH PARTICLE SIZE, VELOCITY AND TRAJECTORY)

Figure A1.– Probability distribution describing the photon detection probability caused by a particle passage through the measuring volume.

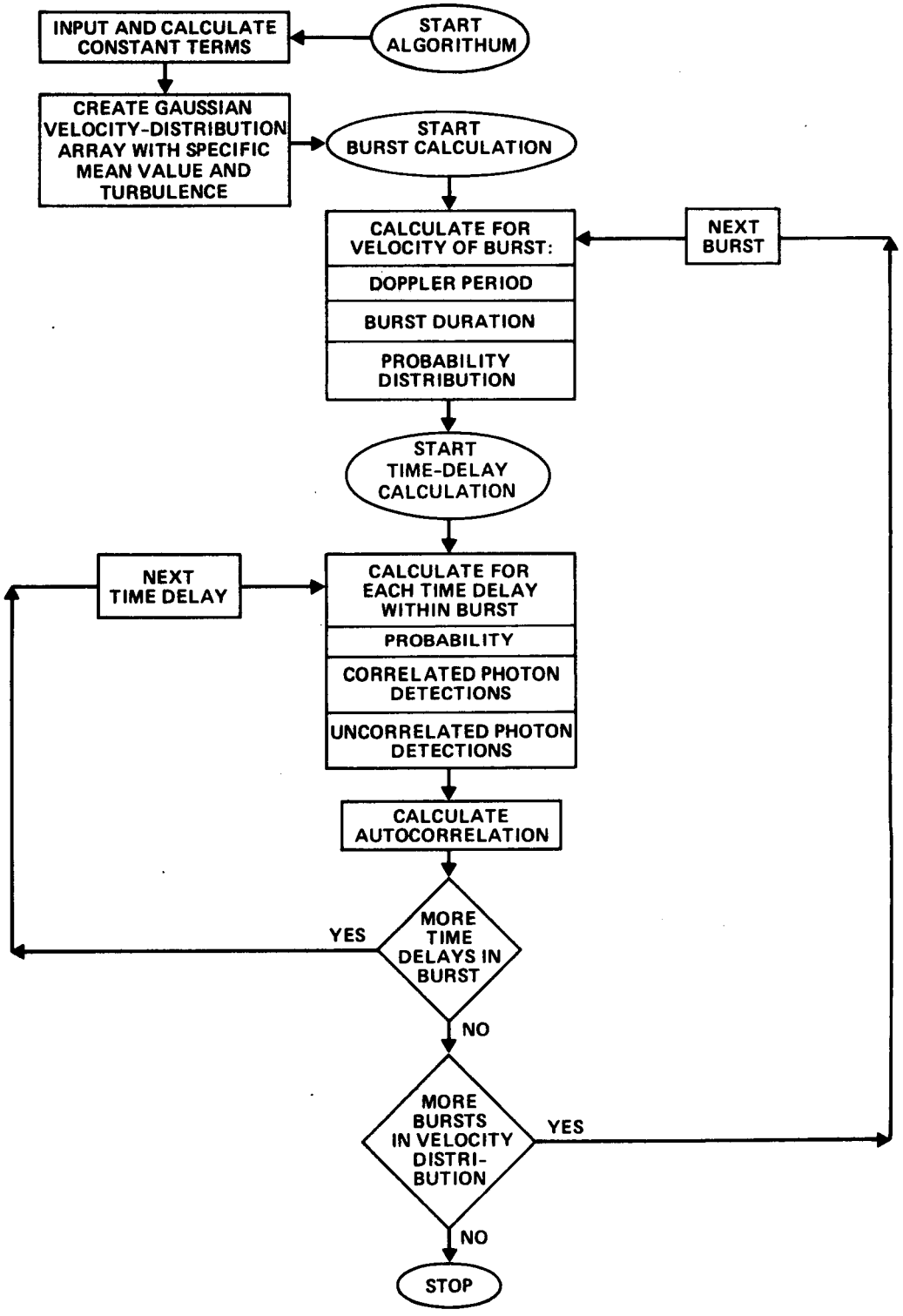

Figure A2.– Flowchart of steps to calculate numerical autocorrelation function.

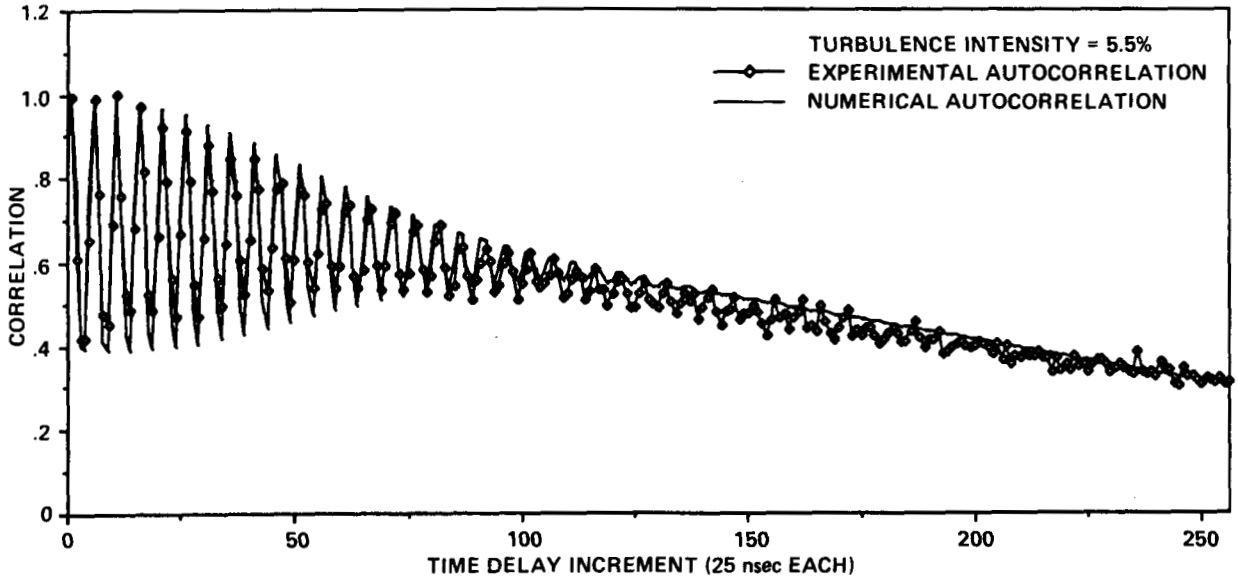

Figure A3.– Autocorrelation functions plotted as a function of time delay for the same turbulence intensity.

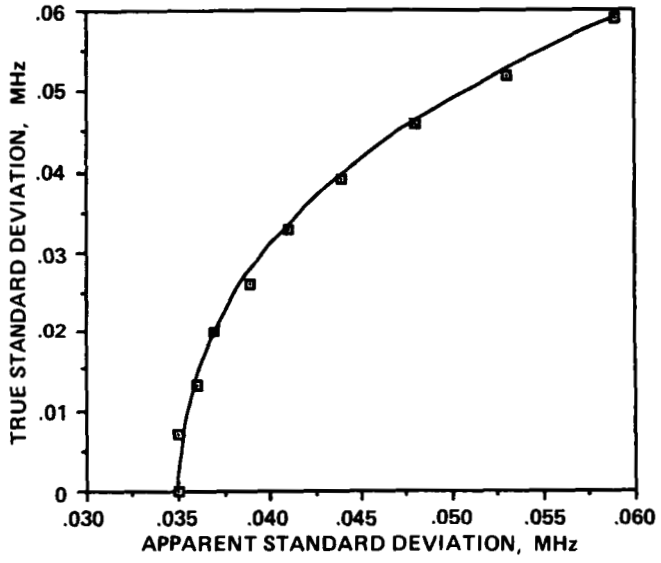

Figure A4.– Correction curve showing true standard deviation plotted against apparent standard deviation for 256 delay cycles at 25 nsec each (line represents curve fit to the data points).

NASA
National Aeronautics and Space Administration

Report Documentation Page

1. Report No.	2. Government Accession No.	3. Recipient's Catalog No.
NASA TM-101081		

4. Title and Subtitle	5. Report Date
A Long-Range Laser Velocimeter for the National Full-Scale Aerodynamics Complex: New Developments and Experimental Application	June 1989
	6. Performing Organization Code

7. Author(s)	8. Performing Organization Report No.
Michael S. Reinath	A-89070
	10. Work Unit No. 505-61-01

9. Performing Organization Name and Address	11. Contract or Grant No.
Ames Research Center Moffett Field, CA 94035	

12. Sponsoring Agency Name and Address	13. Type of Report and Period Covered
National Aeronautics and Space Administration Washington, DC 20546-0001	Technical Memorandum
	14. Sponsoring Agency Code

15. Supplementary Notes

Point of Contact: Michael S. Reinath, Ames Research Center, MS 247-1, Moffett Field, CA 94035
(415) 694-6680 or FTS 464-6680

16. Abstract

A long-range laser velocimeter (LV) developed for remote operation from within the flow fields of the large wind tunnels of the National Full-Scale Aerodynamics Complex is described. Emphasis is placed on recent improvements in optical hardware as well as recent additions to data acquisition and processing techniques. The system has been upgraded from a dual-beam, single-color LV with focal range to 10 m, to a dual-beam, two-color LV with focal range to 20 m. At the new extended measurement range (between 10 and 20 m), signals are photon-resolved, and a photon correlation technique is applied to acquire and process the LV signals. This technique permits recovery of the velocity probability distributions at a particular measurement location from which the mean components of velocity and the corresponding normal stress components of turbulence are obtained. The method used for data reduction is outlined in detail, and a discussion of measurement accuracy is made. To study the performance of the LV and verify the measurement accuracy, laboratory measurements were made in the flow field of a 10-cm-diameter, 30-m/sec axisymmetric jet. Measurements were taken at locations two and four diameters downstream of the exit and at measurement ranges to 10 and 20 m using conventional and photon-correlation data-reduction techniques, respectively. These measured velocity and turbulence intensity surveys are compared to measurements made with a hot-wire anemometer. Additionally, the LV was used during the flow calibration of the 80- by 120-Foot Wind Tunnel to measure the test-section boundary-layer thickness at the maximum wind tunnel speed of 51.5 m/sec. A discussion of the requirements and techniques used to seed the flow is made, and boundary-layer surveys of mean velocity and turbulence intensity of the streamwise component and the component normal to the surface are presented. The streamwise component of mean velocity is compared to data obtained with a total pressure rake.

17. Key Words (Suggested by Author(s))	18. Distribution Statement
Laser velocimeter Laser anemometer Long-range laser velocimetry Wind tunnel instrumentation	Unclassified-Unlimited Subject Category: 35

19. Security Classif. (of this report)	20. Security Classif. (of this page)	21. No. of pages	22. Price
Unclassified	Unclassified	43	A03